The Astrophysical Journal, 617:64–80, 2004 December 10

THE REST-FRAME OPTICAL SPECTRA OF SCUBA GALAXIES

A. M. Swinbank,[1] Ian Smail,[1] S. C. Chapman,[2] A. W. Blain,[2] R. J. Ivison,[3,4] and W. C. Keel[5]

Received 2004 June 24; accepted 2004 August 12

ABSTRACT

We present near-infrared spectroscopy and narrowband imaging at the wavelength of redshifted Hα for a sample of 30 high-redshift, far-infrared luminous galaxies. This sample is selected from surveys in the submillimeter, millimeter, and radio wave bands and has complete redshift coverage with a median redshift of $z \sim 2.4$. We use our data to measure the Hα properties of these systems and to gauge the prevalence of active galactic nuclei (AGNs) in these galaxies through their [N II]/Hα ratios and Hα line widths. Removing obvious AGNs, we find that the predicted Hα star formation rates in this diverse population are suppressed (by a factor of $\sim$10) compared to those derived from their far-infrared luminosities. Using the AGN indicators provided by our near-infrared spectra, we estimate that AGNs are present in at least 40% of the galaxies in our sample. To further investigate this, we construct a composite rest-frame spectrum for both the entire sample and those galaxies that individually show no signs of nuclear activity. We find [N II]/Hα ratios for both composite spectra that suggest that the energy output of the galaxies is star formation rather than AGN dominated. However, we also find that the Hα line in the composite non-AGN spectrum is best fitted with an underlying broad-line component with a narrow/broad flux ratio of 0.45 ± 0.20. The median Hα line width for our sample (removing obvious AGNs) is 400 ± 70 km s^{-1} (FWHM), and the typical spatial extent of the Hα emission in our narrowband observations is $\lesssim$4–8 kpc, which indicates a dynamical mass of $(1-2) \times 10^{11}\ M_{\odot}$ with corresponding dynamical times of 10–20 Myr. Using both high-resolution imaging and spectroscopically identified velocity offsets, we find that seven of the far-infrared luminous galaxies have companions, suggesting that they are undergoing interactions/mergers, and from their relative velocities we can determine a dynamical mass of $(1.5 \pm 0.9) \times 10^{11}\ M_{\odot}$. These measurements are comparable to millimeter CO estimates for the dynamical masses of these systems on similar scales and larger than recent estimates of the dynamical masses of UV-selected galaxies at similar redshifts derived in an identical manner. Using the [N II]/Hα index to predict abundances, we investigate the luminosity-metallicity relation for these galaxies and find that many have metallicities consistent with UV-selected high-redshift galaxies and slightly lower than local luminous infrared and elliptical galaxies (although we caution that our metallicity estimates have possible systematic uncertainties). We also compared our Hα and far-infrared luminosities with deep *Chandra* observations of a subset of our survey fields and use these data to further assess their AGN content. We conclude that these high-redshift, far-infrared luminous galaxies represent a population of massive, metal-rich, merging systems with high instantaneous star formation rates, strong dust obscuration, and actively fueled AGNs that are likely to be the progenitors of massive local elliptical galaxies.

Subject headings: galaxies: active — galaxies: evolution — galaxies: high-redshift — galaxies: starburst — submillimeter

Online material: color figures

1. INTRODUCTION

Recent surveys in the submillimeter, millimeter, and radio wave bands suggest that the star formation density detectable by these dust-independent tracers has evolved strongly with redshift. Indeed, this evolution appears to outstrip that found using tracers that are more sensitive to dust obscuration, suggesting that an increasing proportion of activity in more distant galaxies may be highly obscured (Blain et al. 1999). The populations resolved in these wave bands appear to be responsible for much of the energy density in the extragalactic far-infrared/submillimeter background (Smail et al. 2002; Cowie et al. 2002; Chapman et al. 2004a). However, the extreme faintness of optical counterparts to these obscured galaxies has made it very difficult to obtain accurate redshifts and measure intrinsic properties (e.g., Simpson et al. 2004).

The best-studied examples of the high-redshift, far-infrared luminous galaxy population are those identified in the submillimeter wave band using the SCUBA camera on the James Clerk Maxwell Telescope (JCMT). The median redshift for this population is $\langle z \rangle \sim 2.4$ (Chapman et al. 2003a, 2003b, 2004a), and their submillimeter fluxes suggest that they have bolometric luminosities greater than $10^{12}\ L_{\odot}$, implying that they are ultraluminous infrared galaxies (ULIRGs). The nature of this population and their relevance to models of galaxy formation models and evolution are particularly important (e.g., Genzel et al. 2003; Baugh et al. 2004). If they are powered purely by star formation, then these galaxies form about half of the stars seen locally (Lilly et al. 1999). However, both AGN activity

[1] Institute for Computational Cosmology, Department of Physics, University of Durham, South Road, Durham DH1 3LE, UK; a.m.swinbank@dur.ac.uk.

[2] Astronomy Department, California Institute of Technology, MS 105-24, Pasadena, CA 91125.

[3] Astronomy Technology Centre, Royal Observatory, Blackford Hill, Edinburgh EH19 3HJ, UK.

[4] Institute for Astronomy, University of Edinburgh, Blackford Hill, Edinburgh EH19 3HJ, UK.

[5] Department of Physics and Astronomy, University of Alabama, Box 870324, 206 Gallalee Hall, Tuscaloosa, AL 35487.

and star formation could contribute to their immense far-infrared luminosities, and without further information it is impossible to disentangle the precise energy source (Alexander et al. 2003a).

Rest-frame optical emission line properties provide a powerful tool to investigate star formation rates (SFRs), power sources, and metallicity of galaxies. In particular, the hydrogen Balmer emission line series is one of the primary diagnostics of the SFR in nearby galaxies, with the strength of Hα and its relative insensitivity to extinction making it the line of choice. The nebular recombination lines are a direct probe of the young, massive stellar population, since only stars with masses $\gtrsim$10 $M_{\odot}$ and lifetimes $\lesssim$20 Myr contribute significantly to the integrated ionizing flux. Hence, the strength of these emission lines provides a nearly instantaneous measure of the SFR, independent of the previous star formation history. Moreover, by combining the SFR inferred from this diagnostic line with the far-infrared emission (which comes from reprocessed radiation that has been absorbed and reemitted by dust in the far-infrared at wavelengths of 10–300 μm), we can gauge the prevalence of dust obscuration. The width of the Hα line and its intensity relative to other rest-frame optical lines can also give important information about the presence and luminosity of an AGN within a galaxy (Veilleux & Osterbrock 1987; Veilleux et al. 1995).

Hα is visible in the near-infrared wave band out to $z \sim 2.6$, and projects exploiting the Hα emission at these high redshifts have provided unique insights into the star formation properties of distant galaxies (e.g., Yan et al. 1999; Erb et al. 2003; Shapley et al. 2004; van Dokkum et al. 2004). With precise redshifts for the far-infrared luminous population from the work of Chapman et al. (2004a, 2004b), we can efficiently target the Hα emission from the galaxies to understand the formation and evolution of this population and can identify the power sources, SFRs, metallicities (which are accessible through the [N II]/Hα [N2] index; Pettini & Pagel 2004), and masses, as well as more general issues such as their relation to other classes of high-redshift sources such as Lyman break galaxies (LBGs; Pettini et al. 2001; Erb et al. 2003; Shapley et al. 2004).

As well as measuring the SFR from Hα, it is also possible to measure dynamics of these systems from the same spectra. Far-infrared luminous galaxies at $z \sim 2$ appear morphologically complex (Chapman et al. 2003a; Smail et al. 2004). By measuring the internal dynamics of the galaxies or the velocity offsets between companions, we can also place limits on their masses and so test if these galaxies are truly massive systems (Genzel et al. 2003).

In this paper we present the results from a near-infrared study of a sample of far-infrared–detected galaxies at $z = 1.4$–2.7. We use the Hα emission line to derive their SFRs and dynamics. We investigate the metallicity of these galaxies through their [N II]/Hα emission and dynamics as traced by velocity structures visible in Hα emission in a subset of galaxies. Using *Chandra* data, we also compare our Hα and far-infrared luminosities with X-ray luminosities in several of our survey fields.

In § 2 we present the data reduction and results from the spectroscopic survey and narrowband imaging. In § 3 we discuss the Hα properties of the far-infrared luminous galaxies and present a discussion of the SFRs estimated from their Hα and far-infrared emission and of their dynamics, metallicities, and X-ray counterparts. We present our conclusions in § 4. We use a cosmology with $H_0 = 72$ km s^{-1}, $\Omega_0 = 0.3$, and $\Lambda_0 = 0.7$ in which $1''$ corresponds to 8.2 kpc at $z = 2.4$.

2. OBSERVATIONS AND ANALYSIS

Our target sample comes from two catalogs of far-infrared luminous galaxies by Chapman et al. (2003b, 2004a). The majority of our sample comprises submillimeter-detected, radio-identified galaxies (SMGs). These galaxies have precise positions from the microjansky radio emission and are confirmed to be far-infrared luminous from their detection in the submillimeter/millimeter wave bands with SCUBA or MAMBO. The radio-detected subset of the SMG population represents $\sim$60%–70% of all SMGs brighter than $\gtrsim$5 mJy (Ivison et al. 2002; Chapman et al. 2001; Wang et al. 2004). In addition, we have also included a small number of optical and submillimeter faint radio galaxies (OFRGs) at similar redshifts that have been proposed to be similarly luminous far-infrared galaxies, but with somewhat hotter dust temperatures resulting in them having comparatively faint submillimeter fluxes (Chapman et al. 2004b; Blain et al. 2004). The median redshift of the combined sample is $\langle z \rangle = 2.4 \pm 0.2$. For the purposes of this study we chose targets whose redshifts place Hα in spectral regions that are relatively free from strong atmospheric absorption and emission.

We have explored two routes to investigate the Hα emission from SMGs/OFRGs. First, we used narrowband imaging to assess the Hα fluxes of galaxies in our sample, from both a tunable filter (NSFCAM on IRTF) and more traditional narrowband filters (with the UFTI near-infrared imager on UKIRT) for galaxies whose redshifts serendipitously place Hα in the filter bandwidth. These narrowband observations provide the opportunity to determine the total Hα emission from the SMGs/OFRGs and search for any extended emission or spatial companions.

Second, we used classical long-slit near-infrared spectroscopy with the NIRSPEC spectrograph on Keck and the ISAAC spectrograph on the VLT. These observations allow us to measure precise systemic redshifts for these SMGs/OFRGs, with much higher reliability than that available from their rest-frame UV emission, which frequently show velocity shifts of hundreds of kilometers per second. These precise redshifts are necessary for interferometric CO follow-up of these galaxies (Neri et al. 2003; T. R. Greve et al. 2004, in preparation). The long-slit spectroscopic observations also allow us to measure the Hα luminosities and SFR(Hα) and to gauge the prevalence of AGNs in these galaxies, through the detection of broad lines and extreme [N II]/Hα flux ratios.

These two approaches therefore provide complimentary information on the Hα emission properties of the SMG/OFRG population.

2.1. *Narrowband Imaging*

2.1.1. *IRTF*

Narrowband imaging of five targets was carried out using the NASA Infrared Telescope Facility[6] (IRTF) 3 m Telescope between 2003 April 28 and May 2. The observations were made in generally photometric conditions and $\sim 1''$ seeing. We used the NSFCAM camera (Shure et al. 1993), which employs a 256×256 InSb detector at $0''.15$ pixel^{-1} to give a $38''$ field of view (which probes roughly 300 kpc at $z \sim 2.4$). The continuously variable tunable narrowband filter (CVF) in NSFCAM provides an $R = 90$ passband that was tuned to the galaxy

[6] The Infrared Telescope Facility is operated by the University of Hawaii under Cooperative Agreement NCC 5-538 with the National Aeronautics and Space Administration, Office of Space Science, Planetary Astronomy Program.

TABLE 1
Summary of Narrowband Imaging

Object	λ_{cen} (μm)	t_{exp} (ks) K	t_{exp} (ks) Hα
IRTF tunable filter:			
SMM J105230.73+572209.5	2.3692	2.5	12.6
SMM J123635.59+621424.1	1.9721	1.4	9.0
SMM J131215.27+423900.9	2.3396	1.4	7.2
SMM J140104.96+025223.5	2.3396	0.7	9.0
SMM J163631.47+405556.9	2.1544	4.5	14.4
UKIRT narrowband:			
SMM J105226.61+572113.0	2.248	5.6	22.7
SMM J131232.31+423949.5	2.166	4.0	15.0

Note.—Parameter λ_{cen} denotes the central position of the narrowband filter for the observations.

redshifts measured from the UV spectra from Chapman et al. (2003b, 2004a). Shorter, matched broadband imaging was interspersed between the narrowband exposures to provide continuum subtraction.

The observations were taken in a standard nine-point dither pattern and reduced using a running flat field of the six nearest temporally adjacent frames, masking bright objects before creating the flat-field frame. The final image was made by averaging the flat-fielded frames with a 3 σ clip to reject cosmic rays. To calibrate our data, we observed UKIRT faint photometric standards (Hawarden et al. 2001). These standards were observed at similar air masses and using the same instrumental configuration as the target galaxies. As well as providing good flux calibrations, these observations also allow us to calculate the relative throughput of the narrowband and broadband filters. This allows precise subtraction of the continuum contribution from the Hα emission in the narrowband filter. The NSFCAM CVF filter is wide enough that it contains both the Hα and [N II] emission lines (with the [N II] emission line included at 95% of peak transmission assuming that Hα falls at the peak of the filter trace). The median [N II]/Hα ratio in our spectroscopic sample is 0.25, and we therefore apply a 24% correction to the narrowband flux to account for the [N II] emission line. Exposure times, central wavelengths, and measured Hα fluxes from these observations are given in Tables 1 and 2. We illustrate the Hα morphology for one of the more unusual galaxies in our sample (Fig. 5) and discuss this in more detail in § 3.1.

2.1.2. *UFTI*

We obtained classical narrowband imaging of two SMGs, SMM J105226.61 and SMM J131232.31, whose redshifts should place Hα emission in the Brγ and H_2 S1 filters, respectively. These data were taken with the UFTI near-infrared camera (Roche et al. 2003) on UKIRT[7] on 2003 February 25–27 in $\lesssim$0.″7 seeing and photometric conditions. The UFTI camera has a 1024×1024 HgCdTe array and a plate scale of 0.″091 pixel^{-1}, giving a field of view of $92'' \times 92''$ (which probes roughly 0.75 Mpc in our adopted cosmology). To provide continuum subtraction, we interspersed the narrowband observations with *K*-band imaging. The data were reduced using the ORAC-DR pipeline. The relative throughputs of the broadband and narrowband filters and flux calibration were determined using Two Micron All Sky Survey (2MASS) *K*-band photometry on bright ($K \sim 12$) stars within the 92″ field of view.

All of our narrowband observations were taken based on the rest-frame UV redshifts and assuming that the rest-frame optical redshifts were in agreement. However, a velocity offset of $\sim$500 km s^{-1} between the rest-frame UV and optical emission lines can redshift the Hα out of the narrowband filter. Shifts of the amplitude are relatively rare, and so we assume that our observations have sampled the bulk of the Hα emission in these galaxies.

2.2. *Keck Spectroscopy*

We obtained near-infrared spectra of 24 SMGs/OFRGs using NIRSPEC (McLean et al. 1998) on the 10 m Keck telescope.[8] These observations were obtained on the nights of 2003 August 3, in nonphotometric conditions; in somewhat better conditions on 2004 February 1; and in 0.″5 seeing and in photometric condition between 2004 April 6–9 and 2004 July 31. In all four instances, observations were made using the low-resolution, long-slit mode with a 4 pixel wide (0.″76) slit. Spectra were obtained in the *K* band using the N7 or *K′* filters. In this configuration the resolution is $R \sim 1500$. To subtract sky emission, the observations were made in a standard ABBA sequence, where the object is nodded along the slit by 10″–20″. The total integration times are listed in Table 2 (the integration times of individual exposures were typically $\sim$600 s). One goal of these observations was to provide precise systemic redshifts of the SMGs/OFRGs to compare to those measured in the UV and also to provide a precise redshift for our ongoing CO mapping program on the Plateau de Bure interferometer (Neri et al. 2003; T. R. Greve et al. 2004, in preparation). To maximize the sample size, the exposure times were therefore kept short and so the Hα lines are rarely detected with sufficient signal-to-noise ratio to measure more than their most basic characteristics. We note that the success rate for detecting Hα emission in the SMGs/OFRGs in the near-infrared is $\sim$70%. This estimate is based on the results from the third observing run, which was largely photometric since the first two observing runs were plagued by clouds. In cases in which there was no detection of either continuum or Hα emission, we have assumed that the target was not on the slit (as a result of either an offset error or loss of guiding during the offset from a nearby bright star). In two cases we detected continuum from the target but could not detect any emission lines. In these cases we have quoted upper limits for the Hα luminosity and SFR.

The spectroscopic observations were reduced using the WMKONSPEC package in IRAF. We remap the two-dimensional spectra using linear interpolation to rectify the spatial and spectral dimensions. After subtracting pairs of nod positions, residual sky features were removed in IDL using sky regions on either side of the object spectrum. The wavelength calibration from the 2003 run used the night sky lines, while for the 2004 observing runs we used an argon arc lamp. The output pixel scale is 4.3 Å pixel^{-1}, and the instrumental profile has an FWHM of 15 Å (measured from the widths of the sky lines). In

[7] The United Kingdom Infrared Telescope is operated by the Joint Astronomy Centre on behalf of the UK Particle Physics and Astronomy Research Council.

[8] Obtained at the W. M. Keck Observatory, which is operated as a scientific partnership among the California Institute of Technology, the University of California, and the National Aeronautics and Space Administration. The Observatory was made possible by the generous financial support of the W. M. Keck Foundation.

TABLE 2

SUMMARY OF RESULTS

Object	t_{exp} (ks)	z	Hα Flux (10^{-19} W m^{-2})	FWHM$_{rest}$ (km s^{-1})	EW$_{rest}$ (Å)	SFR(Hα) ($M_\odot$ yr^{-1})	[N II]/Hα	L(FIR) ($10^{12}L/L_\odot$)	Class (UV/Hα)
Spectroscopy									
NIRSPEC Keck:									
SMM J030227.73+000653.5	3.0	1.4076 [2]	15.2 ± 2.0	420 ± 15	85 ± 10	140 ± 18	1.38 ± 0.07	$5.78^{+2.44}_{-0.82}$	SB/AGN
RGJ 030258.94+001016.3	2.0	2.2404 [8]	1.8 ± 0.5	327 ± 22	360 ± 110	51 ± 15	1.13 ± 0.40	$7.74^{+1.41}_{-1.41}$	int/AGN
RGJ 105154.24+572325.0	4.8	1.681 [8]	2.7 ± 1.9	1565 ± 250	91 ± 6	61 ± 40	<0.2	$2.80^{+0.35}_{-0.35}$	SB/AGN
SMM J105158.02+571800.3	2.4	2.2390 [4]	2.4 ± 1.2	257 ± 44	21 ± 5	57 ± 15	<0.1	$10.40^{+1.90}_{-1.00}$	SB/SB
SMM J105207.56+571904.7	4.8	2.692 [2]	1.3 ± 0.4	285 ± 20	21 ± 4	217 ± 64	0.18 ± 0.10	$9.46^{+2.70}_{-2.70}$	SB/SB
SMM J105230.73+572209.5	2.4	2.6100 [3]	1.2 ± 0.3	171 ± 40	10 ± 3	42 ± 15	<0.05	$10.29^{+0.75}_{-1.12}$	SB/SB
SMM J123549.44+621536.8	2.4	2.2032 [3]	15 ± 1	536 ± 33	184 ± 9	239 ± 18	0.50 ± 0.10	$6.76^{+1.50}_{-1.12}$	SB/int
SMM J123600.15+621047.2	1.2	2.0017 [2]	3.7 ± 0.3	305 ± 12	91 ± 8	126 ± 8	0.20 ± 0.10	$10.50^{+1.50}_{-1.50}$	SB/SB
SMM J123606.85+621021.4	2.4	2.5054 [8]	2.0 ± 0.3	612 ± 35	28 ± 5	78 ± 12	<0.2	$8.70^{+1.80}_{-1.20}$	SB/int
SMM J123621.27+621708.4	2.4	1.9924 [7]	2.0 ± 0.6	586 ± 92	212 ± 25	56 ± 16	0.20 ± 0.15	$12.76^{+1.50}_{-2.25}$	SB/int
SMM J123622.65+621629.7	2.4	2.4662 [5]	3.4 ± 0.6	434 ± 25	137 ± 40	125 ± 20	<0.05	$9.01^{+1.88}_{-2.03}$	SB/SB
SMM J123635.59+621424.1	1.8	2.0150 [2]	4.2 ± 0.3	240 ± 33	45 ± 10	130 ± 30	0.67 ± 0.27	$7.47^{+1.50}_{-1.50}$	AGN/AGN
			6.9 ± 0.9	1623 ± 213	73 ± 10				Broad-line component
SMM J123707.21+621408.1	3.6	2.490 [5]	1.6 ± 0.5	348 ± 40	35 ± 8	88 ± 24	...	$5.48^{+2.03}_{-1.58}$	SB/SB
SMM J123711.32+621331.3	2.4	1.9958 [4]	0.4 ± 0.3	112 ± 18	10 ± 5	16 ± 9	<0.05	$5.48^{+2.03}_{-1.58}$	int/SB
SMM J123711.98+621325.7	2.4	...	<0.25	...	<5	<6	...	$3.88^{+1.05}_{-0.82}$	SB/...
SMM J131205.60+423946.0	2.4	...	<0.3	...	<6	<8	...	$5.50^{+2.00}_{-2.00}$	SB/...
RGJ 131208.34+424144.4	2.4	2.2372 [18]	0.9 ± 0.2	448 ± 60	24 ± 5	32 ± 18	1.20 ± 0.60	$5.13^{+1.05}_{-1.05}$	SB/AGN
			0.9 ± 0.8	959 ± 100	26 ± 5				Broad-line component
SMM J131208.82+424129.1	2.4	1.5439 [6]	6.1 ± 2.3	387 ± 60	103 ± 15	111 ± 32	0.20 ± 0.15	$3.23^{+0.15}_{-0.19}$	SB/AGN
			2.1 ± 1.0	450 ± 80	120 ± 20				Broad-line component
RGJ 131236.05+424044.1	2.4	2.2402 [8]	2.3 ± 1.2	447 ± 75	20 ± 6	106 ± 40	0.22 ± 0.08	$6.69^{+0.59}_{-0.59}$	SB/SB
SMM J163639.01+405635.9	2.4	1.4880 [6]	8.9 ± 3.0	248 ± 25	188 ± 35	147 ± 48	0.30 ± 0.20	$5.47^{+1.88}_{-1.50}$	SB/SB
SMM J163650.43+405734.5	4.8	2.3850 [5]	12.2 ± 2.0	306 ± 47	105 ± 20	58 ± 19	0.41 ± 0.10	$50.5^{+15.0}_{-15.8}$	int/AGN
			12.0 ± 1.0	1753 ± 238	1236 ± 200				Broad-line component
SMM J163655.80+405914.0	2.4	2.5918 [6]	2.4 ± 0.4	225 ± 29	336 ± 60	102 ± 15	0.45 ± 0.10	$10.9^{+2.25}_{-3.76}$	AGN/AGN
			16 ± 2	2962 ± 402	254 ± 40				Broad-line component
SMM J163658.19+410523.8	2.4	2.4482 [6]	1.9 ± 0.4	364 ± 77	76 ± 15	71 ± 35	0.65 ± 0.3	$10.90^{+2.25}_{-3.76}$	SB/SB
SMM J163706.51+405313.8	2.4	2.3745 [9]	4.7 ± 0.6	225 ± 29	96 ± 15	160 ± 20	0.27 ± 0.04	$7.17^{+4.21}_{-3.00}$	AGN/AGN
			2.7 ± 0.8	3317 ± 987	125 ± 15				Broad-line component
ISAAC VLT:									
SMM J221733.91+001352.1	3.0	2.5510 [7]	8.5 ± 3.5	198 ± 98	30 ± 10	254 ± 128	...	$4.94^{+1.88}_{-2.63}$	SB/SB
Narrowband Imaging									
NSFCAM IRTF:									
SMM J105230.73+572209.5	12.6	2.610 [5]	1.2 ± 0.5	...	...	21 ± 8	...	$10.3^{+0.75}_{-1.13}$	SB/...
SMM J123635.59+621424.1	9.0	2.005 [5]	8.1 ± 1.0	...	...	181 ± 20	...	$7.47^{+1.50}_{-1.50}$	AGN/...
SMM J131215.27+423900.9	7.2	2.565 [5]	11.8 ± 1.0	...	...	493 ± 41	...	$13.90^{+0.53}_{-2.48}$	AGN/...
SMM J140104.96+025223.5	9.0	2.565 [5]	1.2 ± 0.2	...	...	47 ± 10	...	$6.76^{+2.50}_{-2.50}$	AGN/...
SMM J163631.47+405546.9	14.4	2.283 [5]	0.30 ± 0.19	...	...	10 ± 6	...	$10.97^{+6.76}_{-4.73}$	AGN/...
UFTI UKIRT:									
SMM J105226.61+572113.0	22.7	2.425 [5]	0.78 ± 0.1	...	...	27 ± 4	...	$2.40^{+1.40}_{-1.40}$	SB/...
SMM J131232.31+423949.5	15.0	2.300 [5]	1.9 ± 0.1	...	...	58 ± 5	...	$14.80^{+0.98}_{-2.93}$	SB/...

NOTES.—The value given in the square brackets in the third column is the error in the last decimal place. The Hα flux given in the fourth column is the narrow-line Hα flux unless otherwise stated. The Hα fluxes are the observed flux (not corrected for slit flux losses or atmospheric transmission), but the SFRs have had both corrections applied (where applicable). The Hα SFRs are uncorrected for extinction. Hα classifications are described in § 2.4.

all line widths quoted in the following sections we have deconvolved the instrumental profile from the FWHM of the galaxies.

The redshifts of our targets have been relatively well constrained from rest-frame UV spectroscopy carried out with LRIS on the Keck telescope. However, again we stress that the rest-frame UV and optical emission lines can show velocity offsets of a few hundred kilometers per second (Pettini et al. 2001; Erb et al. 2003; Shapley et al. 2003; I. Smail et al. 2004, in preparation). With knowledge of the UV redshift we were able to identify the Hα and [N II] emission in each spectrum and ensure the correct line identification.

As the first two and final observing runs were nonphotometric, we calibrate the integrated Hα fluxes onto an absolute flux scale by careful comparison of the spectra with the *K*-band photometry of the galaxies (Smail et al. 2004). We convolve the galaxy spectra with the normalized *K*-band filter response curve to obtain the mean flux conversion factor for each galaxy spectrum. We also note that the atmospheric transmission at the wavelength of redshifted Hα is $\sim$1 for all targets except SMM J123621.27, where the transmission is 0.75 ± 0.02. For the third observing run we used a standard star (FS 27) to flux-calibrate the data. We also use the broadband photometry to flux-calibrate these data in order to verify that the process applied to calibrate the previous observations is reliable and obtain a mean ratio of calibration factors of 1.05 ± 0.10. This gives us confidence that using the photometry to flux-calibrate gives consistent results. All of the objects included here have detectable continuum emission. Where the continuum or emission lines are faint, we binned the reduced two-dimensional frames by a factor of 2 in both the spatial and spectral dimension to improve the contrast prior to extraction. We show the extracted spectra for the whole sample in Figure 1.

2.3. *ISAAC VLT Spectroscopy*

During the night of 2003 October 21, observations of SMM J221733.79 were obtained in queue mode with the ISAAC spectrograph on the VLT[9] (Moorwood 1997). The data were taken using the medium-resolution ($R = 3000$) grating and a 1″ slit (with an instrumental FWHM of $\sim$6.7 Å) and in 0.″8 seeing. In this configuration the output pixel scale is 1.2 Å pixel^{-1}. The total integration time was 3.0 ks with the data taken in 4×750 s exposures in the standard ABBA sequence where the object is nodded along the slit by 10″–20″ to achieve sky subtraction. We reduced the data using the ISAAC data reduction pipeline, which rectifies, flat-fields, and wavelength-calibrates the two-dimensional frames. Prior to extraction, the data were binned by a factor of 2 in the spectral direction to boost the contrast of the object. We observed the standard star HIP 032007 for flux calibration. The derived Hα fluxes and redshifts are listed in Table 2, and the spectra are shown in Figure 1.

2.4. *Spectral Analysis*

To accurately determine the redshift for each galaxy, we fit both the continuum level and emission lines Hα λ6562.8 and [N II] $\lambda\lambda$6548.1, 6583.0 simultaneously with a flat continuum plus Gaussian profiles using a χ^2 fit and taking into account the greater noise in regions of strong sky emission. As well as fitting the narrow-line Hα and [N II] emission, we also attempt to identify any underlying broad-line Hα (AGN) component by fitting a broad Gaussian profile at the same redshift as the narrow-line Hα emission but only accepting the result if the χ^2 fit is significantly better (with greater than 90% confidence limit) than with no broad-line component. This allows us to deconvolve the narrow-line Hα flux, which may arise from star formation, from the broad-line Hα flux from an AGN. For the observations that were flux-calibrated using the *K*-band photometry we estimate the errors in the Hα flux and continuum levels using both the uncertainty in the *K*-band magnitude and the errors on the best fit to the emission line, evaluated by varying the fit by $\Delta\chi^2 = 1$. The error bars on the emission-line fluxes and equivalent widths are therefore conservative errors that take into account the error in using the *K*-band photometry and the uncertainty that arises from the signal-to-noise ratio in the data. This flux error is propagated through to the SFR. We list the parameters for the fits for narrow (and where relevant broad) components in Table 2, along with their uncertainties. We note that the [S II] $\lambda\lambda$6716, 6731 doublet is detected in at least three individual spectra: SMM J123600.00, SMM J163650.43, and SMM J163639.01.

The ratio of [N II] to Hα line fluxes from our spectra, as well as the presence of a broad component, can be used to identify luminous AGNs in these galaxies (e.g., Veilleux & Osterbrock 1987; Armus et al. 1989). We measure all of these observables from our spectra and use them to flag galaxies whose Hα and far-infrared luminosities could be affected by emission from an AGN, rather than being star formation dominated (Table 2). Using the [N II]/Hα emission line ratio and Hα line width as diagnostics, we separate our sample into three classes: AGN dominated, intermediate, and systems whose properties are consistent with star formation (but may still contain some AGNs). In a later section we test the reliability of these classes through the use of deep X-ray observations. We classify galaxies whose near-infrared spectra show $[\mathrm{N\ II}]/\mathrm{H}\alpha < 0.7$ and $\mathrm{FWHM_{rest}} < 500$ km s^{-1} as starbursts (SBs). Galaxies with $\mathrm{FWHM_{rest}}$ between 500 and 1000 km s^{-1} are classified as intermediate, while galaxies with $[\mathrm{N\ II}]/\mathrm{H}\alpha > 0.7$ and/or $\mathrm{FWHM_{rest}} > 1000$ km s^{-1} are classified as AGNs. Using this classification, $\sim$40% (9/24) of the objects in our detected spectroscopic sample have some indication of an AGN (most classifications are based on Hα line widths, with only one AGN changing classification if we remove the limits on [N II]/Hα). This is similar to the rate estimated from UV spectroscopy and high-resolution radio imaging (Chapman et al. 2003a, 2003b, 2004c). By comparing the rest-frame UV and optical spectral classifications (Table 2), we find that the 15 galaxies identified as SBs in the rest-frame UV are classified as SB (9), AGN (3), and intermediate (3) from their rest-frame optical spectra. Likewise, the three AGNs identified in the rest-frame UV are all classified as AGNs from their rest-frame optical spectra. We conclude that these classifications are in reasonable agreement. However, we note that their AGNs could be easily hidden from view in both wave bands (see, e.g., § 3.5). Looking at the far-infrared luminosities of the three spectral classes, we find median values of $(5.2 \pm 3.0) \times 10^{12}$, $(6.6 \pm 0.7) \times 10^{12}$, and $(5.4 \pm 1.4) \times 10^{12}$ $L_\odot$ for the SMGs/OFRGs classed as AGN, SB, and intermediate, respectively. We thus find no strong evidence for a strong luminosity dependence of the different spectral classes.

To determine total Hα fluxes, we have also corrected for slit losses based on the average *K*-band light distribution of the galaxies. As we know the position, width, and orientation of the spectroscopic aperture for each galaxy, we use the *K*-band images to calculate the fraction of the total *K*-band light that

[9] Based on observations collected with the ESO VLT-UT1 Antu Telescope (072.A-0156).

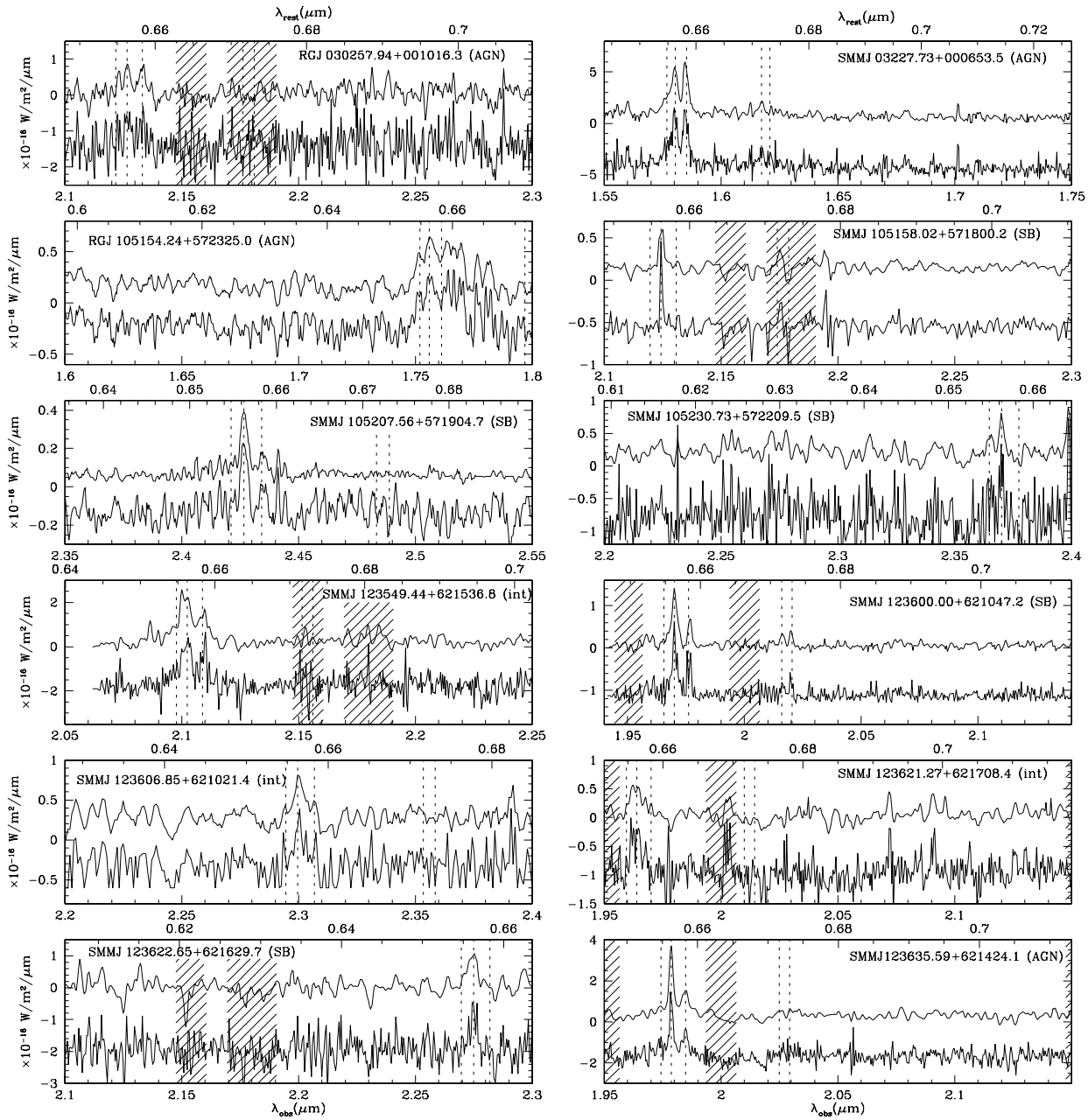

FIG. 1.—Hα spectra for the SMGs/OFRGs in our sample. The lower spectrum in each panel is the raw spectrum (offset in flux scale for clarity). The upper spectrum is smoothed to the instrumental resolution. The dashed vertical lines show the positions of the Hα λ6562.8, [N II] $\lambda\lambda$6548.1, 6583.0, and [S II] $\lambda\lambda$6717, 6731 emission lines. The lower axis scale shows the observed wavelength, while the upper scale displays the rest-frame wavelength. The shaded areas are regions of strong sky emission. The spectra are ordered in right ascension range as in Table 2, and we label each galaxy with its spectral classification from § 2.4. Note that we identify two Hα emission lines from SMM J123707.21 rather than Hα + [N II] (see § 3.1). The final spectra are higher resolution ISAAC/VLT spectra (Table 2).

enters the spectroscopic aperture. The galaxies are frequently extended and disturbed (e.g., Smail et al. 2004), and while this correction is uncertain, we view it as more reliable to apply this factor before comparing Hα to far-infrared SFRs, rather than to ignore it. However, we note that using a single factor for correcting slit losses may contribute some scatter when comparing the Hα and far-infrared SFRs. By careful comparison of a simulated slit for each galaxy in our sample with the *K*-band imaging, we estimate the fraction of the flux entering the slit compared to the total *K*-band flux of the galaxy, *f*, and obtain a mean value of $f = 0.62 \pm 0.06$. We assume that the equivalent width of the Hα emission line is constant across the galaxy and so only those galaxies with spectra taken in photometric conditions, whose flux calibration was carried out using the standard-star observations, require this correction to their Hα flux.

Finally, we note that there are two repeated observations of targets between the spectroscopic and narrowband imaging samples, SMM J105230.60 and SMM J123635.59, as well as narrowband imaging of SMM J140104.96 for which an Hα spectrum exists in the literature [$(0.56 \pm 0.08) \times 10^{-18}$ W m^{-2}; Ivison et al. 2000]. The agreement between the Hα fluxes from the two techniques is very good (Table 2), with a median ratio of spectroscopic to imaging fluxes of 0.96 ± 0.04. On the basis of this good agreement we feel confident in combining the spectroscopic and narrowband imaging data to discuss the Hα luminosities of SMGs/OFRGs in the following sections.

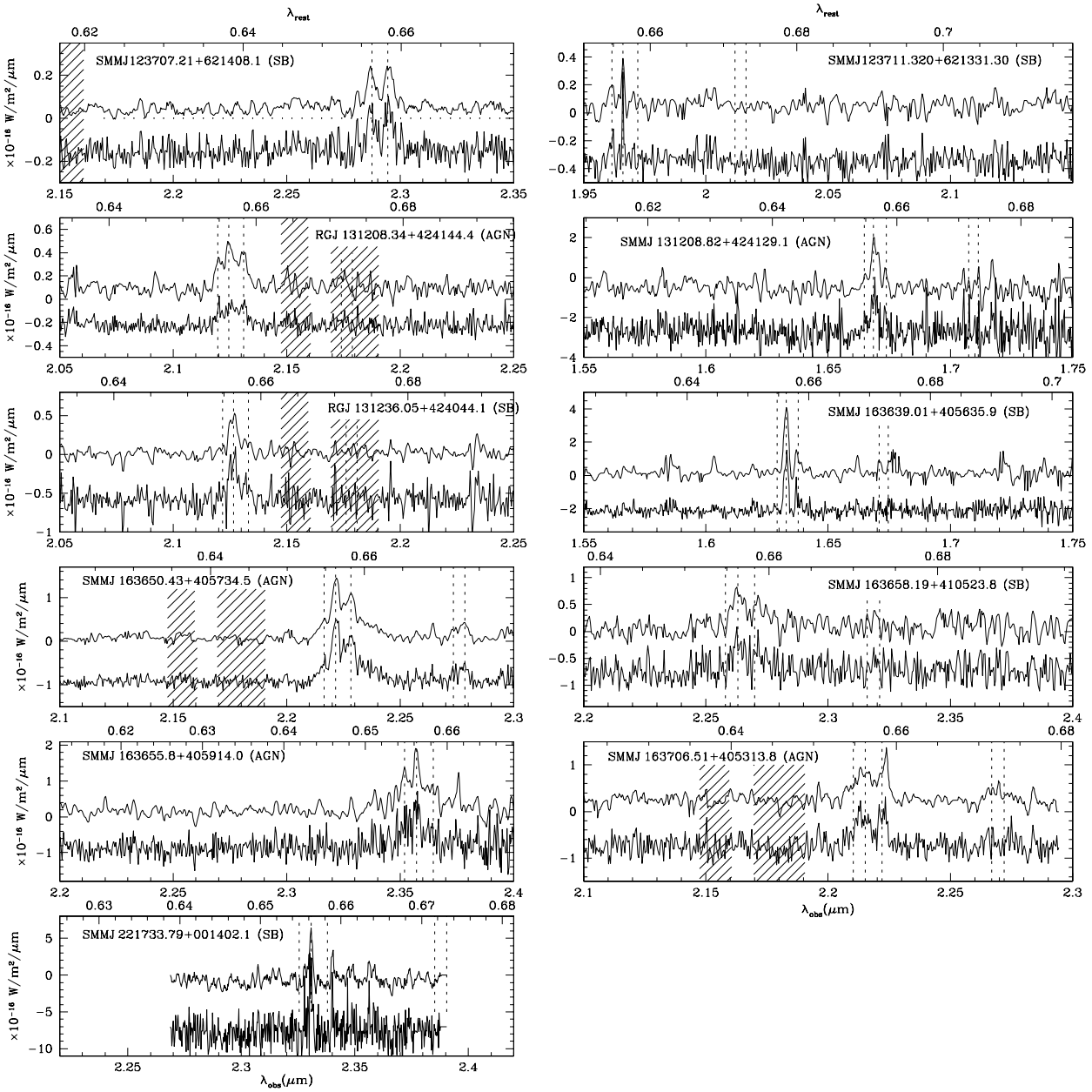

FIG. 1.—*Continued*

2.5. *Star Formation Rates*

For solar abundances and adopting a Salpeter initial mass function (IMF), the conversion between Hα flux and SFR is $\mathrm{SFR}(M_\odot\ \mathrm{yr}^{-1}) = 7.9 \times 10^{-35} L(\mathrm{H}\alpha)$ W (Kennicutt 1998). This calibration assumes that all of the ionizing photons are reprocessed into nebular lines (i.e., they are neither absorbed by dust before they can ionize the gas, nor do they escape the galaxy).

We also have a second SFR indicator for our sample of SMGs/OFRGs: their far-infrared (FIR) luminosities. A significant fraction of the bolometric luminosity of the most active dusty galaxies is absorbed by interstellar dust and reemitted in the thermal IR, at wavelengths 10–300 μm. If young stars dominate the radiation output in the UV-visible wave band and the dust opacity is high everywhere, then the far-infrared luminosity measures the bolometric luminosity of the starburst and this in turn provides an excellent tracer of the SFR of the galaxy. Adopting the models of Leitherer & Heckman (1995) for continuous bursts of age 10–100 Myr and using the same IMF as in the Hα calculation yields $\mathrm{SFR}(M_\odot\ \mathrm{yr}^{-1}) = 4.5 \times 10^{-37} L(\mathrm{FIR})$ W (Kennicutt 1998). We stress that this relation only holds if the age of the starburst is less than 100 Myr.

We list the SFR and Hα flux measurements from our sample in Table 2. We also give the far-infrared luminosities of these galaxies from Chapman et al. (2003b, 2004b). These values are derived from fitting model spectral energy distributions (SEDs) to the observed 850 μm and 1.4 GHz fluxes of the galaxies at their known redshifts, assuming that the local far-infrared–radio correlation holds (Condon et al. 1991; Garrett 2002).

3. RESULTS AND DISCUSSION

3.1. *Notes on Individual Galaxies*

Observations of six of the galaxies in our sample are particularly noteworthy, and so we discuss these in more detail here.

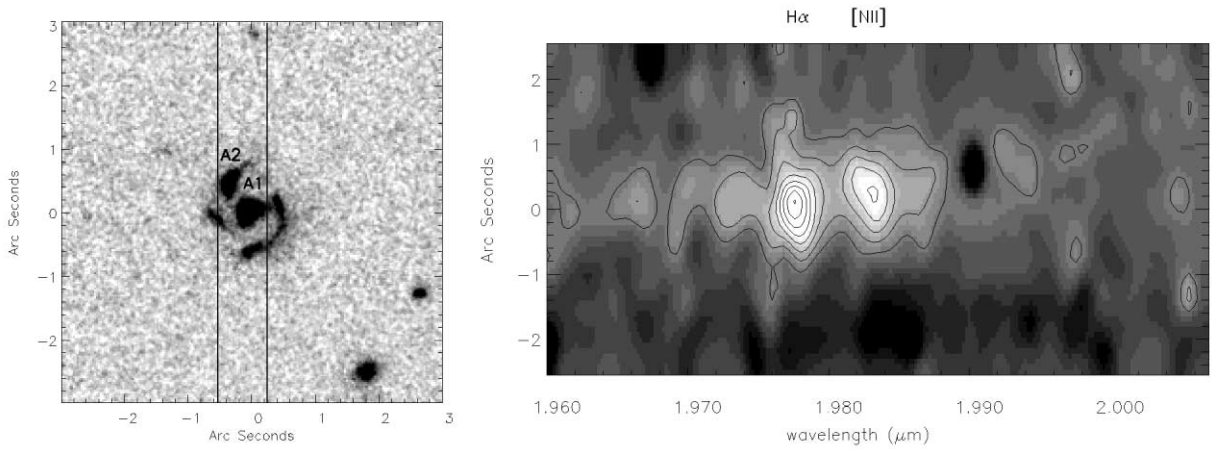

FIG. 2.—*Left*: Combined *B*-, *V*-, and *I*-band *HST* ACS observations of SMM J123635.59+621424.1 with the slit position overlaid. *Right*: Position-velocity diagram around the Hα line from the NIRSPEC near-infrared spectrum of the galaxy. This shows an apparent $\sim$100 km s^{-1} velocity gradient in the Hα emission line and a somewhat larger velocity gradient, $\sim$150 km s^{-1}, in [N II]. The central component of the galaxy (labeled A1) has an [N II]/Hα ratio of 0.60 ± 0.15 and hosts a bright, unresolved radio source (Chapman et al. 2004a); both features suggest that it contains an AGN. A1 is offset from A2 by $\sim$150 km s^{-1} in velocity and around 3 kpc in projection on the sky. A2 has an [N II]/Hα ratio of 0.2 ± 0.1, suggesting that this is a star-forming knot or close companion. Here $1''$ corresponds to 8.4 kpc at the redshift of this galaxy and the image has been rotated to match the position angle of the spectrum.

SMM J123635.59+621424.1.—Dawson et al. (2003) identified this object as a $z = 2.015$ spiral galaxy, but their near-infrared spectroscopy around the Hα emission line shows a 2500 ± 250 km s^{-1} broad-line Hα component and [N II]/Hα emission line flux ratio 0.45 ± 0.1. The presence of the broad-line component and detection of hard ($\Gamma = 0.3$) X-ray emission from *Chandra* imaging indicate an obscured type II AGN (Dawson et al. 2003). Our spectroscopic and narrowband observations of this galaxy produce comparable Hα fluxes, which, along with the compact morphology of the galaxy in the IRTF narrowband image, suggests that the spectroscopic slit is sampling the bulk of the emission from this system (the slightly lower flux in the narrowband observation arises because the narrow filter only samples the narrow-line Hα; $\sim$20% of the broad-line flux is missed). Our spectroscopic observations of this target show clear velocity structure in the Hα and [N II] emission lines (Fig. 2). We aligned the slit with the center of the galaxy and the bright knot (labeled A2 in Fig. 2), and our resulting Keck spectroscopic observations indicate either a velocity shear or rotation in the Hα emission line with an amplitude of $\sim$100 km s^{-1} within $\sim 2''$ (17 kpc in projection) along the slit (Fig. 2). By collapsing down the Hα and [N II] emission lines in the spectral direction, we find an offset of $0''.3$ (3 kpc) along the slit between the maximum intensities of these two lines, as well as an associated variation in the [N II]/Hα ratio from $\sim 0.2 \pm 0.1$ up to $\sim 0.60 \pm 0.15$ (which is consistent with the results of Dawson et al. 2003). We also find a similar broad-line component to the Hα emission, confirming the presence of an AGN. The high-resolution *Hubble Space Telescope*[10] (*HST*) ACS image of this galaxy (Fig. 2), from the GOODS imaging of this region (Giavalisco et al. 2004; Dawson et al. 2003; Smail et al. 2004), shows an apparently face-on spiral galaxy with a bright nucleus (A1) and a prominent companion or knot in one of the spiral arms (A2); the optical extent of the galaxy is 13 kpc ($1''.5$). The separation between the nucleus (A1) and knot (A2) in the image is $\sim 0''.5$ (5 kpc), comparable to the apparent offset in the emission-line peaks. The high-resolution 1.4 GHz MERLIN map of this galaxy in Chapman et al. (2004c) shows an unresolved radio source coincident with the nuclear component, which is also where the [N II]/Hα is the strongest ($\sim$0.6), providing further support for the classification of this component as an AGN. The face-on aspect of this system, combined with the modest velocity difference between A1 and A2, suggests to us that the latter may be a dynamically distinct component (rather than a star-forming knot inside a spiral arm), an interaction that has prompted the activity we see. We note that it is possible for intensity gradients between separate components to mimic velocity gradients as a result of the way in which long-slit spectroscopy mixes spatial and spectral domains. However, the spatial offset between A1 and A2 in the dispersion direction is $\sim 0''.4$, corresponding to 10 Å, which is much less than the apparent velocity gradient. We therefore suggest that the velocity offset most likely arises from motions within the galaxy, rather than as an artifact of the observation.

SMM J123707.21+621408.1.—We observed this target with a position angle such that the NIRSPEC slit passes through the two components shown in the *HST* ACS imaging in Smail et al. (2004). This galaxy consists of a red component and a much bluer object separated by $0''.2$ (1.7 kpc; labeled B1 and B2 in Fig. 3). The resulting NIRSPEC spectrum shows two strong, spatially extended lines separated by $\sim$600 km s^{-1}. We identify both of these emission lines as Hα (rather than Hα and [N II]) from two separate components for two reasons: (1) the spatial separation between the two components in the spectra is matched almost exactly by the separation in the *HST* ACS image (Fig. 3); and (2) if the higher velocity component was identified as strong [N II] λ6583, then the line ratio would be [N II]/H$\alpha \sim 1$, and yet we see no signs of the [S II] emission line, which has a ratio of [S II]/[N II] ~ 0.5 for AGNs (Ferland & Osterbrock 1986).

SMM J123711.32+621331.3.—This target was known to consist of two radio sources, both of which may contribute to the far-infrared emission. Aligning the slit along both components, we detect only faint continuum and no lines from the UV-identified component, SMM J123711.98+621325.7, for which Chapman et al. (2004a) measured the redshift of the system. However, we do detect Hα emission from the second

[10] Based on observations made with the NASA/ESA *Hubble Space Telescope*, which is operated by STScI for the Association of Universities for Research in Astronomy, Inc., under NASA contract NAS5-26555.

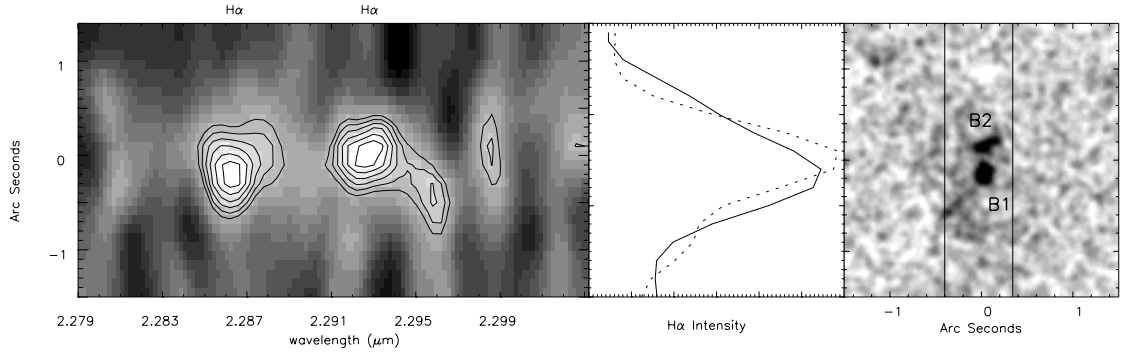

FIG. 3.—*Left*: Position-velocity diagram around the Hα line from the near-infrared spectrum of SMM J123707.21. *Right*: Combined *B*-, *V*-, and *I*-band *HST* ACS observations of this galaxy with the slit position overlaid. *Middle*: Intensity distribution of the Hα emission collapsed over the central 200 km s^{-1} of each of the two Hα emission lines. This shows an apparent spatial offset of 0.″2 (and 600 km s^{-1} velocity offset) between the two galaxies. This matches the apparent separation of the central component of the galaxy (labeled B1) from the much redder second component (labeled B2), which are offset by 2 kpc in projection. (For a color version of this image, see Smail et al. 2004.)

radio source, SMM J123711.32+621331.3. This allowed us to derive a redshift of 1.9958 ± 0.0004, giving an offset of 400 ± 50 km s^{-1} and 8″ (∼70 kpc) in projection from SMM J123711.98+621325.7.

RGJ 131236.05+424044.1.—The ground-based *K*-band imaging of this galaxy from Smail et al. (2004) shows a bright nucleus surrounded by a diffuse halo approximately 2″ (16 kpc) in extent. The two components seen in the near-infrared spectrum are separated by $\sim 185 \pm 45$ km s^{-1} in velocity and 0.″4 (3.4 kpc) in projection. The two-dimensional near-infrared spectrum suggests that one of the sources (labeled C1) displays signs of a velocity shear in Hα across ∼0.″5. The [N II]/Hα ratio shows marginal evidence for variation from 0.45 ± 0.10 to 0.35 ± 0.10 between C1 and C2 and also mimics the velocity offset between C1 and C2. These modest [N II]/Hα emission line ratios indicate that both components are likely to be starburst, rather than AGN, dominated.

SMM J140104.96+025223.5.—This $z = 2.56$ submillimeter-selected galaxy (SMM J14011+0252) is discussed in detail by Ivison et al. (2000, 2001). It lies in the field of the $z = 0.25$ cluster A1835 and is expected to be amplified by a factor of 2.75 by the foreground cluster potential. The morphology of this galaxy is complex (Fig. 4). Ivison et al. (2001) identify three main components: J1, a blue relatively smooth and regular object; J2, a bluer and more compact object about 2″ to the west of J1; and J1n, an extremely red, diffuse structure that extends 2″–3″ to the north of J1.

The interpretation of this multicomponent system is contentious. Ivison et al. (2001) suggest that the gas reservoir and source of the far-infrared emission from this galaxy reside in J1n, with J2 and J1 simply being less obscured components within the same system. However, Downes & Solomon (2003) suggest that the clumpy features to the southwest of J1 (called J1se), as well as J1n and J2, are all images of a single, highly amplified background submillimeter source, which is being lensed by both the regular component of J1 (which they identify as a foreground [$z \sim 0.20$] galaxy) and the cluster potential.

Our IRTF continuum-subtracted Hα image provides a powerful tool for testing these competing suggestions (see also Tecza et al. 2004). We compare the morphology of the Hα emission with the R_{702}- and *K*-band images in Figure 5. It is clear that the bulk of the emission traces components J1 and J1se, with the regular J1 and compact J2 being undetected. This immediately rules out the possibility that J2 is a lensed counterimage of J1n or J1se. However, the absence of Hα emission from the smooth component of J1 is a concern, suggesting that the claim by Downes & Solomon (2003) that it is a foreground lens may be correct. To further test this, we have returned to the optical spectrum of J1 presented by Barger et al. (1999) and claimed by them to represent a classical LBG. More

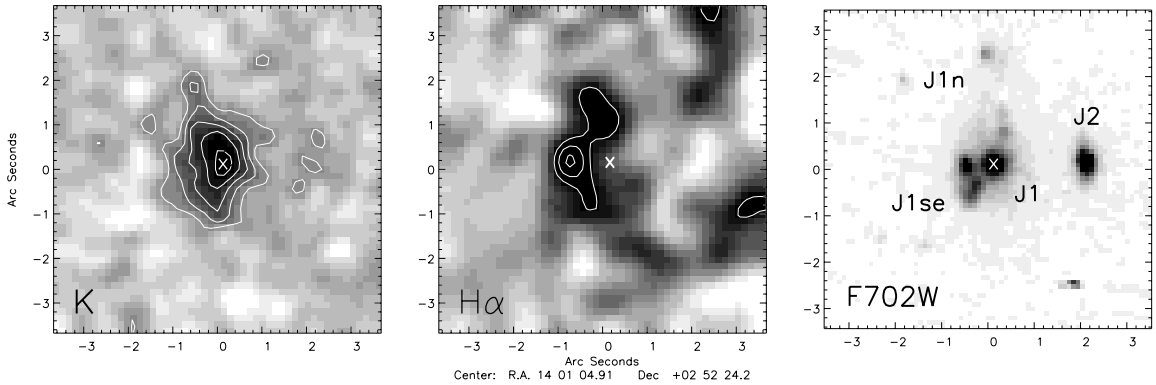

FIG. 4.—Three views of SMM J140104.96: broadband *K* image from IRTF (*left*); Hα continuum-subtracted, narrowband image from IRTF (middle); and the *HST* R_{702} band of the system, which illustrates its very complex morphology (*right*). We identify in the *HST* image the three main components of this galaxy as defined by Ivison et al. (2001), and in each panel we also mark the position of the peak of component J1. It is clear that the optical–near-infrared colors and Hα surface brightness of component J2 are much different from those of J1n and J1se, ruling out the suggestion that J2 represents a lensed counterimage of J1n or J1se (Downes & Solomon 2003). Moreover, the Hα emission extending south from J1n and wrapping around J1 traces the morphology of the clumps visible in the *R* band, J1se, and has no significant contribution from the smooth component, J1. We discuss the interpretation of this result in more detail in § 3.1.

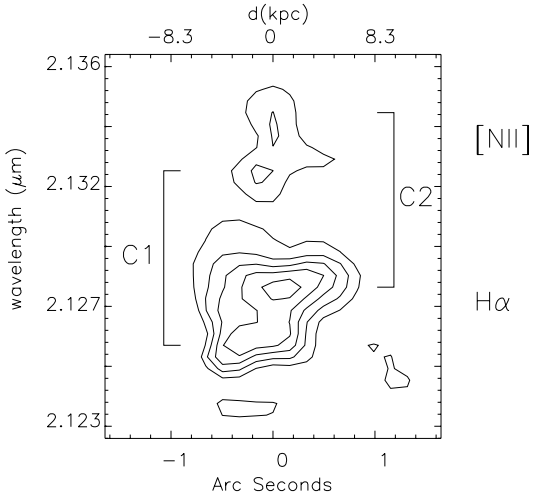

FIG. 5.—Two-dimensional near-infrared spectrum of RGJ J131236.05, showing the velocity structure seen in Hα and [N II]. We identify two components (labeled C1 and C2), offset by 185 ± 40 km s^{-1} and 3.4 kpc in projection along the slit.

careful study of this spectrum leads us to reexamine this interpretation: there are strong absorption features at 4745, 4784, 4912, 4957, 5374, and 6070 Å, which are unidentifiable at the redshift claimed by Barger et al. (1999), $z = 2.55$, but correspond exactly to Balmer Hζ, Hη, Ca H and K, G-band, and Hβ absorption at $z = 0.248$. This is an unfortunate conjunction: J1 is a $\sim 0.1L^*$, poststarburst member of the A1835 cluster. The absence of any strong emission lines in this galaxy and broadband colors that are much bluer than the typical passive E/S0 cluster member mean that its nature is not immediately obvious from either the published spectrum or the true color images of the cluster (Ivison et al. 2000, 2001).

How does this effect the interpretations of SMM J140104.96 by Downes & Solomon (2003) and Ivison et al. (2001)? We confirm that J1 is a foreground lens as stated by Downes & Solomon (2003). However, our observations disprove their central claim that J1n, J1se, and J2 are highly amplified multiple images of an intrinsically low-luminosity submillimeter source. In fact, J1n/J1se and J2 are probably single images of three background galaxies at $z = 2.56$ (see Tecza et al. 2004), with the Hα emission from this system arising entirely from very red J1n/J1se, which is also the site of a massive gas reservoir and hence most likely the far-infrared source (Frayer et al. 2003; Ivison et al. 2001). The addition of J1 to the foreground lens model does increase the estimate of the area-averaged amplification for J1n/Jse from 2.5 to $\sim$5; however, this does not significantly alter any of the conclusions in Ivison et al. (2001).

SMM J163650.43+405734.5.—We also observed SMM J163650.43 (ELAIS N2 850.4; Smail et al. 2003) using NIRSPEC for a total of 4.8 ks at two orthogonal position angles. The detailed kinematics of this complex merging system using three-dimensional near-infrared spectroscopy will be discussed in A. M. Swinbank et al. (2004, in preparation). However, we note that the broad Hα component is apparently offset from the narrow Hα component by $\sim$300 km s^{-1}. The redshift quoted in Table 2 is that of the narrow-line Hα.

3.2. Hα *Properties of SMGs*

We show near-infrared spectra of the 23 detected galaxies from our Keck and VLT observations in Figure 1 marked with the expected redshifts of lines based on the best-fit Hα redshift (Table 2). As these were short exposures, primarily meant to derive redshifts, the signal-to-noise ratio on the individual galaxies is generally modest. To overcome this, we have also combined all of the spectra to provide a composite near-infrared spectrum for a representative far-infrared luminous galaxy at $z \sim 2.4$.

We create the composite spectrum by deredshifting and summing all of the spectra (normalized by Hα flux) for our galaxies (we note that stacking the spectra based on their individual signal-to-noise ratio or an unweighted stack does not alter any of the conclusions below). We also derive a composite spectrum for those galaxies that individually show no signs of an AGN (i.e., those with small [N II]/Hα ratios and line widths). The resulting composite spectra are shown in Figure 6. The rest-frame composite spectrum from the entire sample is best fitted (>99% confidence level) with an underlying broad-line region with a narrow-line–to–broad-line flux ratio of 0.6 ± 0.1 and $\mathrm{FWHM_{rest}}$ of 1300 ± 210 km s^{-1} for the broad-line Hα and 325 ± 30 km s^{-1} for the narrow-line Hα. The average [N II]/Hα for the entire sample is 0.42 ± 0.05, which is indicative of star formation.

The [S II]/Hα ratio can be used to classify the spectral type of galaxies (Veilleux et al. 1995). The wavelengths of the [S II] $\lambda\lambda$6716, 6731 lines in the composite spectra are 6722 ± 6 and

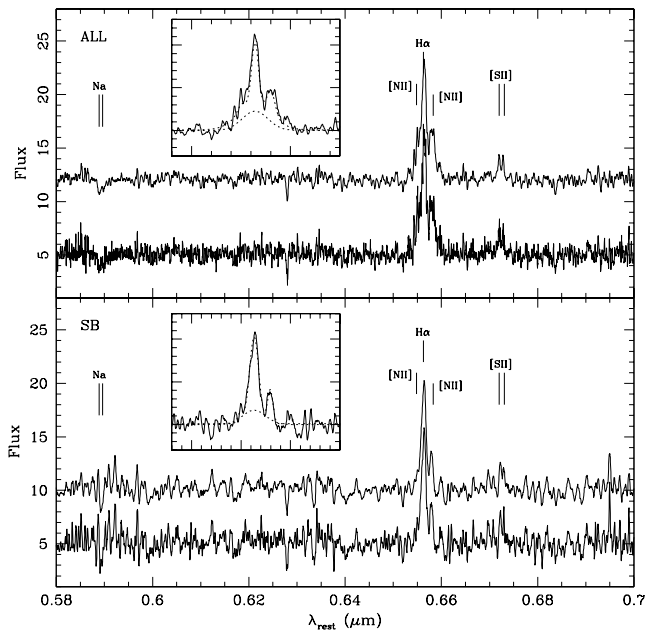

FIG. 6.—Rest-frame composite spectrum of all of the galaxies in our sample (*top*) and the composite from the (individually spectroscopically classified) star-forming galaxies (*bottom*; we have not included SMM J123707.21 in either composite as we believe that the spectra display two Hα components coming from two interacting galaxies rather than Hα and [N II]). The insets show the region around the Hα emission line with the best fit to the emission line using four Gaussian profiles overlaid. We also show the broad-line component of the best fit. The average [N II]/Hα ratio is 0.42 ± 0.05 for the entire sample and 0.19 ± 0.05 for the star-forming galaxies. Both are consistent with star-forming galaxies rather than an AGN. We also detect the [S II] $\lambda\lambda$6716, 6731 emission doublet (marginally detected in the SB sample) and the (unresolved) stellar Na $\lambda\lambda$5889.95, 5895.92 absorption doublet. By fitting the Na absorption and [S II] doublets, we find no velocity offset from Hα. The [S II]/Hα ratio can be used to classify the SMG/ORFG optical emission line properties as LINER or H II region like. While the SMGs/OFRGs that are individually classified as star-forming galaxies show no signs of an underlying broad Hα line, the composite from this subsample of galaxies is best fitted with a narrow/broad Hα emission line ratio of 0.45 ± 0.20. [*See the electronic edition of the Journal for a color version of this figure.*]

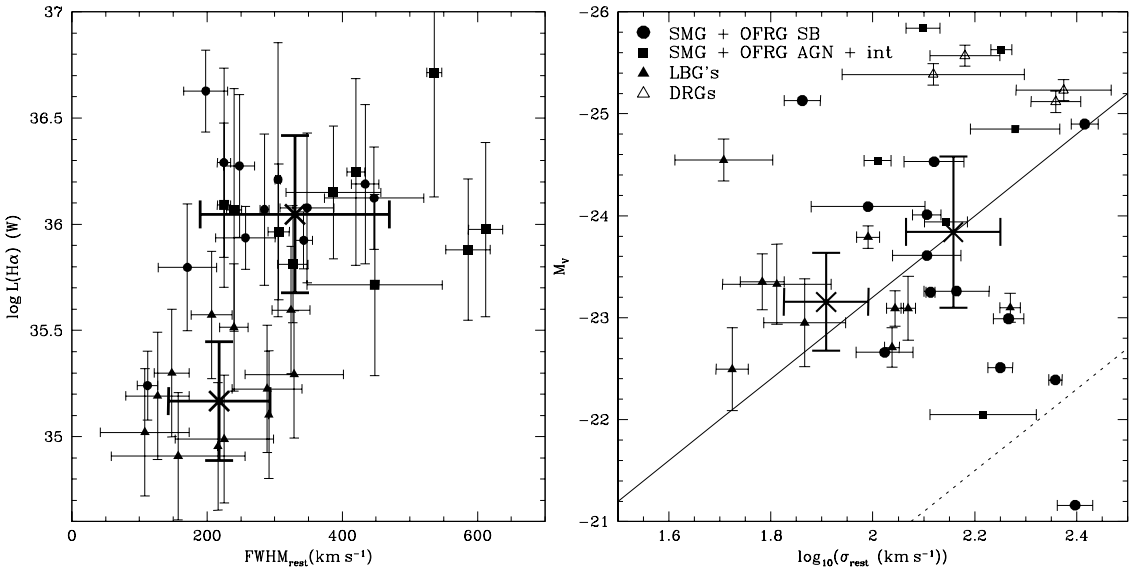

FIG. 7.—*Left*: Comparison of the Hα luminosity vs. FWHM$_{rest}$ for the narrow Hα components (deconvolved for instrumental resolution) in our sample compared to those found in UV-selected galaxies by Erb et al. (2003; we have conservatively assumed a factor of 2 uncertainty in the Hα luminosities for this sample). We also include those galaxies that show single broad lines (no narrow component). The crosses mark the positions of the median luminosity and FWHM$_{rest}$ for the two populations. The line widths in the SMGs/OFRGs have a median of 330 km s^{-1} and a long tail out to $\sim$600 km s^{-1}. In comparison to the UV-selected galaxies studied by Erb et al. (2003) (which have a median of $\sim$210 km s^{-1}), SMGs/OFRGs appear to be typically more massive systems, with a wider distribution of line widths (although some of the broadest lines may come from unresolved companions or AGNs). *Right*: Correlation between rest-frame optical emission line width and rest-frame *V*-band luminosity (the Faber-Jackson relation) for the SMGs/OFRGs compared to the LBGs and DRGs from Pettini et al. (2001) and van Dokkum et al. (2004). The crosses mark the positions of the median luminosity and σ_{rest} for the SMGs/OFRGs and LBGs. We show the local Faber-Jackson relation by the dotted line (assuming $V - R = 0.3$) and also the same line offset by a further 2.5 mag in order to pass through the median of the SMG sample (*solid line*). [*See the electronic edition of the Journal for a color version of this figure.*]

6729 $\pm$ 5 Å, indicating no detectable velocity offset between the Hα and [S II] emission lines. From the strengths of the lines we estimate a ratio of [S II]/Hα = 0.10 $\pm$ 0.04, placing the composite SMG/OFRG within either the LINER or H II region of the classification space (Veilleux & Osterbrock 1987; Veilleux et al. 1995). This is similar to the typical optical spectral classification of local ULIRGs, for which mid-infrared observations (Lutz et al. 1999) and spatially resolved spectroscopy (Heckman et al. 2000) both suggest that star formation is the dominant power source (see Lutz et al. 1999).

The composite spectrum also shows an absorption feature at a wavelength close to that expected for the Na doublet that is seen from cool stars and from the warm neutral ($T \sim 10^4$ K) phase of the interstellar medium (ISM; Phillips 1993). This has been used to map the velocity structure of large-scale outflows from nearby ULIRGs (Heckman et al. 2000; Rupke et al. 2002). For a galaxy whose light is dominated by a young starburst, as we believe is the case for these SMGs/OFRGs, the warm ISM is expected to be the primary source of this absorption feature. We fit the Na absorption line with two Gaussian profiles with a fixed separation and variable width and derive a central wavelength of 5889 $\pm$ 5 Å, which is entirely consistent with the rest-frame wavelength of the resolved doublet ($\lambda\lambda$5889.95, 5895.92). We thus place a limit of less than 150 km s^{-1} on the possible velocity offset of this feature from the Hα redshift. The FWHM$_{rest}$ of the Na lines is 292 $\pm$ 192 km s^{-1}, which is also consistent with the FWHM of the Hα emission in the rest-frame composite.

The composite spectrum thus shows no signs of an offset in velocity between Na or [S II] and Hα. This is slightly surprising since many local luminous/ultraluminous infrared galaxies display velocity offsets of several hundred kilometers per second between these lines (Heckman et al. 2000; Rupke et al. 2002). We defer a detailed discussion of the velocity offsets between the UV ISM and (starburst) nebular emission lines in the individual galaxies to a later paper (I. Smail et al. 2004, in preparation).

Turning to the rest-frame composite from those galaxies that individually show no signs of an AGN component (i.e., those with low [N II]/Hα emission line ratios and small Hα line widths), we fit this spectrum with both [N II] $\lambda\lambda$6548, 6583 emission lines and also attempt to fit a broad-line Hα component. When the broad component is included in the fit, the total χ^2 is marginally better than when the broad component is excluded, with a change in the total $\chi^2 = 4$ that corresponds to $\sim$2 σ (or $\sim$87% confidence). The resulting best-fit model for the SB composite has an underlying broad-line Hα component with a ratio of broad-line/narrow-line Hα = 0.45 $\pm$ 0.20 and a broad-line FWHM$_{rest}$ = 890 $\pm$ 210 km s^{-1}, suggesting that even the SMGs/OFRGs that are identified individually as starbursts may contain at least some level of underlying nonthermal activity. Nevertheless, the [N II]/Hα emission line ratio is 0.19 $\pm$ 0.05, which, along with the limit of [S II]/Hα $\lesssim$ 0.14, still suggests that the energy output is star formation, rather than AGN, dominated.

3.3. *Kinematics of* Hα *Emission*

The narrow Hα emission line of the SB composite has a rest-frame FWHM$_{rest}$, after correcting for the instrumental resolution of the observations, of FWHM$_{rest}$ = 400 $\pm$ 70 km s^{-1}, in agreement with the average Hα line width from the SMGs/OFRGs that make up this composite spectrum (350 $\pm$ 50 km s^{-1}). This is somewhat larger than the Hα line widths of UV-selected galaxies at $z \sim 2$ identified by Erb et al. (2003), who derive a mean FWHM$_{rest}$ = 242 $\pm$ 65 km s^{-1} for their sample. We compare the distribution of line widths for these two populations (as a function of their Hα luminosities) in Figure 7. We see that the SMGs/OFRGs are typically 6 times brighter in

Hα (*before* any correction for reddening) than the UV-selected population at their epoch. More interestingly, the emission-line widths of the SMGs/OFRGs are on average $\sim$50% larger than those measured for the UV-selected systems, although the two distributions overlap substantially. This difference could reflect either (1) different halo masses, (2) different dynamical states, (3) a contribution from a broad AGN component in some SMGs/OFRGs, or (4) starburst-driven superwinds contributing to the line widths. The composite spectra from § 3.2 certainly suggest that an unidentified broad component to the Hα emission may be present in some SMGs/OFRGs; however, as we show below, we do not believe that this is the chief cause of the difference in the line widths of the two populations.

We first compare our Hα-derived line widths with those obtained from the dynamics of cold gas as traced by interferometric maps of the CO distributions in a small number of SMGs (Frayer et al. 1999; Neri et al. 2003; Genzel et al. 2003). The sample of five galaxies compiled by Neri et al. (2003) have an $\mathrm{FWHM_{rest}}$ for the CO of 420 ± 35 km s^{-1} and a mean ratio of Hα to CO FWHM consistent with unity (1.27 ± 0.24) for the four galaxies in common with our sample. The CO line widths are unaffected by the presence of any AGN or large-scale winds, and so this suggests that the AGN or superwind contribution to the Hα line widths for SMGs/OFRGs may not be responsible for the comparatively large Hα line widths.

We can therefore combine the emission-line widths for our sample with the typical physical extent of the Hα emission from our narrowband imaging of the SMGs/OFRGs to place limits on their masses. The spatial extent of the Hα in the galaxies has a wide distribution: $\lesssim$0.″5–1.″0 (corrected for seeing) or $\lesssim$4–8 kpc (cf. Smail et al. 2004). Assuming that the Hα emission arises from virialized clouds in the galaxy's potential well, we estimate a typical mass of $(1-2)\times10^{11}\ M_{\odot}$ for the SMGs/OFRGs in our sample (Erb et al. 2003), with corresponding dynamical times of 10–20 Myr. Using the limits on the spatial extent of the CO emission, Neri et al. (2003) determine a median dynamical mass of $\sim6\times10^{10}\ M_{\odot}$ assuming that the CO gas is in bound orbits. Thus, the masses derived from the dynamics of the cold gas in a small sample of these galaxies support those estimated from the emission-line kinematics.

The masses of UV-selected galaxies at $z\sim2$ derived in an identical manner by Erb et al. (2003) have a median of $(3.3\pm1.1)\times10^{10}\ M_{\odot}$, around 5 times lower than our estimates for the SMGs/OFRGs. This is due to a combination of smaller estimated sizes and lower Hα line widths. Clearly both of these estimates have large systematic errors, yet they are suggestive of a real difference in the characteristic masses (or dynamical states) of rest-frame UV- and far-infrared–selected galaxies at $z\gtrsim2$.

We can also obtain an independent measure of the masses of the SMGs/OFRGs from the seven galaxies that show multiple components and for which we have estimates of the velocity differences between the components. Assuming random orientations on the sky and that the components are bound/merging, the masses of the systems are $\sim(1.5\pm0.9)\times10^{11}\ M_{\odot}$. This is comparable to the earlier estimates and gives us confidence that the SMGs/OFRGs are indeed massive galaxies.

3.4. *Magnitude–Line Width Correlations*

Correlations between rest-frame luminosity and kinematics (as measured by the widths of the emission lines) at high redshift have had only limited success. Pettini et al. (2001) and van Dokkum et al. (2004) have attempted to study the Tully-Fisher–like or Faber-Jackson–like (Tully & Fisher 1977; Faber & Jackson 1976) correlation for LBGs and distant red galaxies (DRGs) at $z\gtrsim2$; however, no correlations have been found over the range $\mathrm{FWHM_{rest}}\sim120-300$ km s^{-1}. This may be due in part to the small sample sizes involved. To search for such a correlation, the SMGs for which we have well-defined narrow-line Hα line width measurements can be added to this sample. We compute the dereddened rest-frame *V*-band magnitudes for the SMGs in our sample by using HyperZ (Bolzonella et al. 2000) to compute the best-fit SED to the observed *IJK* photometry from Smail et al. (2004). We also convert $\mathrm{FWHM_{rest}}$ to σ by assuming $\mathrm{FWHM}=2.35\sigma$.

Figure 7 shows the resulting luminosity–line width correlation for the combined sample of SMGs, LBGs, and DRGs (the latter two from Pettini et al. 2001 and van Dokkum et al. 2004 are corrected for reddening using their estimates of A_V). We also overlay the local Faber-Jackson relation from Jørgensen et al. (1995a, 1995b, 1999; assuming $V-R=0.3$) and fit the zero point of the same correlation so that it passes through the median of the SMG sample, resulting in an offset of 2.5 mag. This offset is comparable to the $\Delta_{\mathrm{fade}}V$ found in Smail et al. (2004) and suggests that the descendants of these high-redshift populations are likely to lie on or around the local Faber-Jackson relation.

3.5. *SFR Comparisons*

Next we compare the far-infrared and Hα luminosities of the galaxies in our sample to investigate the influence of AGN and star formation power sources and the possible effects of dust extinction on the Hα emission from this population.

Figure 8 compares the Hα and far-infrared luminosities of the galaxies in our sample. We have also included measurements from the literature from five well-studied dusty, high-redshift galaxies: SMM J02399−0136 (Ivison et al. 1998, 2000), SMM J17142+5016 (Smail et al. 2003), ERO J164502+4626 (Dey et al. 1999), SMM J04431+0210 (Frayer et al. 2003), and SMM J16359+6612 (Kneib et al. 2004).

The SFR derived from the far-infrared and Hα should be correlated if the effects of dust and any contributions from AGNs are uniform across the sample. The SMGs/OFRGs in our sample show only a weak correlation between SFR(FIR) and SFR(Hα), with comparable scatter in the Hα-derived SFR and that estimated from the far-infrared [$\Delta(\mathrm{FIR})/\mathrm{FIR}=0.30\pm0.18$ vs. $\Delta(\mathrm{H}\alpha)/\mathrm{H}\alpha=0.37\pm0.20$]. Reassuringly, the two galaxies for which we failed to obtain Hα detections in good conditions are also two of the least luminous galaxies when ranked on their far-infrared emission.

We have also included in Figure 8 samples of similar and less luminous far-infrared galaxies from surveys of the $z<1$ universe. These come from ISOCAM-selected galaxy surveys (Franceschini et al. 2003; Flores et al. 2004) and studies of local very luminous and ultraluminous infrared galaxies by Poggianti & Wu (2000) and Dopita et al. (2002). Compared to these samples, we see a similar wide dispersion in the ratio of far-infrared to Hα luminosities across a factor of nearly 100 in far-infrared luminosity. This is suggestive of a similar diversity in the energy sources and obscuration for galaxies with far-infrared luminosities from 10^{10} to $\gtrsim10^{12}\ L_{\odot}$. In support of this, we note that the distribution of Hα EWs (Table 2) for the SMG sample peaks at about $\sim$20–40 Å and has a long tail out to $\gtrsim$100 Å, with a median $\mathrm{EW}(\mathrm{H}\alpha)=75\pm25$ Å. The shape of the distribution is very similar to that seen for the rest-frame Hα EWs of local ULIRGs from Veilleux et al. (1999), which have a median $\mathrm{EW}(\mathrm{H}\alpha)=73\pm8$ Å, suggesting that the unobscured/partially observed mix of emission-line gas and

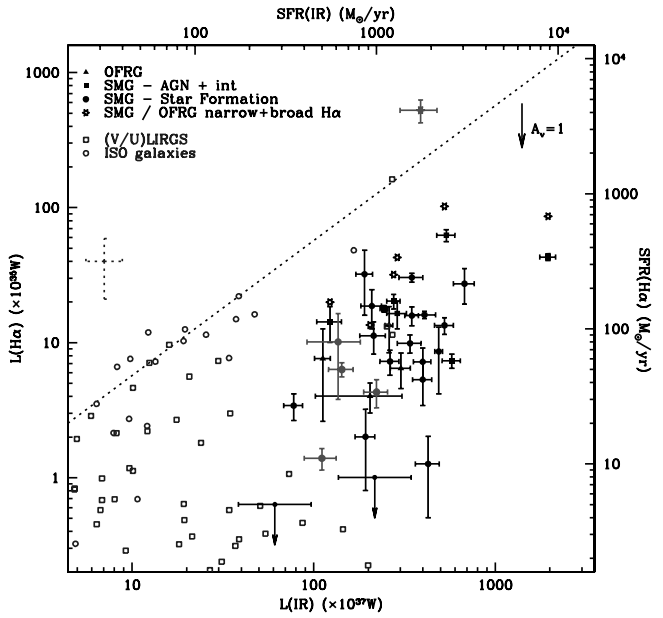

FIG. 8.—Comparison of the far-infrared vs. narrow-line Hα luminosities and SFRs in our data with those in local samples. We include in the plot the SFRs for the SMGs/OFRGs when the broad-line Hα flux is included in the estimate (the galaxies classified as intermediate in § 2.4 are included with the AGN classification). This is more comparable to the quantities calculated for local samples. We also include the previously published SMGs (Kneib et al. 2004; Dey et al. 1999; Smail et al. 2003; Frayer et al. 2003; Ivison et al. 1998). The dotted line represents identical estimated SFR from Hα and far-infrared. The sample is compared to the results from ISOCAM, including the $z = 0.2-1.5$ galaxies in the Hubble Deep Field–South by Franceschini et al. (2003) and the local luminous infrared galaxy sample ($z = 0.2-0.7$) by Flores et al. (2004). We also compare the data to the very luminous and ultraluminous infrared galaxy sample of local *IRAS* greater than 2 Jy sources by Dopita et al. (2002) and Poggianti & Wu (2000). We include a representative error bar from the comparison samples on the left side of the plot. [*See the electronic edition of the Journal for a color version of this figure.*]

stellar continuum is comparable to local ULIRGs (although we note that the projected size of the spectroscopy apertures in the local ULIRGs is less than 1 kpc, whereas for the SMGs/OFRGs the projected size is ~10 kpc; thus, some caution should be taken when comparing the two samples).

Our SMG/OFRG sample is intrinsically luminous in the far-infrared, but their Hα flux (and estimated SFR) is much less than expected with a median SFR(Hα) compared to SFR(IR) of 94 ± 20 and $1380 \pm 190\ M_{\odot}\ \mathrm{yr}^{-1}$, respectively. Overall, the Hα SFRs are suppressed by at least a factor of 10 relative to that suggested by the far-infrared. In comparison to other far-infrared–selected samples, we see that the SMGs/OFRGs extend the trend for proportionally less Hα luminosity in more far-infrared luminous galaxies. As we have shown, there is no detectable difference between the far-infrared luminosities of the starburst- and AGN-classed galaxies in our sample, suggesting that this declining ratio of Hα to far-infrared emission is unlikely to be caused by an increasing AGN contribution. Hence, we attribute the variation to copious and increasing amounts of dust enshrouding the galaxy and extinguishing Hα emission.

Unfortunately, the wavelength coverage of our spectroscopic observations does not extend to Hβ, and thus the reddening in these galaxies cannot be estimated directly from the Balmer decrement to confirm this suggestion, although attempts at estimating the reddening in this manner are underway for a subsample of galaxies. The only target with an Hβ measurement in the literature is SMM J123707.21+621408.1 (Simpson et al. 2004), with an Hβ flux of $(2.1 \pm 0.9) \times 10^{-20}$ W m^{-2}. The Hα/Hβ flux ratio is 8 ± 6, which corresponds to a reddening of $A_V = 1.4 \pm 1.0$ (Calzetti et al. 1994); the large uncertainties arise from the modest signal-to-noise ratio detections of both Hα and Hβ emission lines. For the rest of the sample, we have attempted to derive the reddening for these galaxies from their broadband optical/near-infrared colors (Smail et al. 2004). These are derived by using the HyperZ photometric redshift code (Bolzonella et al. 2000) to fit young continuous star formation models with variable reddening and age to the galaxy photometry at their known redshifts. We find a median reddening of $A_V = 3.0 \pm 1.0$. Accounting for the contribution of Hα to the *K*-band photometry may decrease this estimate slightly, but the reddening estimated from the continuum colors indicates substantial extinction at the wavelength of Hα (assuming that the continuum and line emission arise from the same regions in the galaxy). The scatter of a factor of 2.5 is more than sufficient to explain the dispersion in the strength of the Hα emission at a fixed far-infrared luminosity. We conclude therefore that the large scatter in SFR(FIR)/SFR(Hα) probably arises from two main factors: (1) there is a range in the continuum extinction in the more far-infrared luminous population, and (2) the morphological diversity of submillimeter-selected galaxies, which includes a large fraction of interacting or merging systems, sometimes with highly obscured components, may lead to a large variation in the in-slit Hα fluxes for these systems (Chapman et al. 2003a; Smail et al. 2004).

3.6. *Metallicities*

Rest-frame optical emission lines from extragalactic H II regions provide an important diagnostic of the chemical evolution of galaxies since their properties reflect the makeup of the ISM. Moreover, feedback processes from short-lived massive stars in high-SFR galaxies may be responsible for the enrichment of the intergalactic medium with heavy metals over a wide range of redshifts (Heckman et al. 2000; Adelberger et al. 2003). For star-forming and irregular galaxies the correlation between metallicity (traced by oxygen abundances, O/H) and rest-frame luminosity is well established in the local universe and spans a factor of over 100 in (O/H) and at least 8 mag in M_V. The correlation is in the sense that more massive (and luminous) galaxies exhibit a higher degree of metal enrichment (Garnett et al. 1997; Zaritsky et al. 1994; Garrett 2002; Lilly et al. 2003; Lamareille et al. 2004). If such a correlation exists at high redshift, then it may be more important for understanding the present distribution of metals in the universe, since the bulk of the star formation activity in the most massive and active galaxies is thought to occur at $z > 1$ (Blain et al. 1999).

Since we lack the observations necessary to calculate the R_{23} index (Zaritsky et al. 1994) for our sample, we turn to the N2 index described by Storchi-Bergmann et al. (1994) and discussed more recently by Denicolo et al. (2002) and Pettini & Pagel (2004). This indicator is defined at $\mathrm{N2} = \log([\mathrm{N\ II}]\ \lambda6584/\mathrm{H}\alpha)$ and is calibrated to the oxygen abundance (O/H) via $12 + \log(\mathrm{O/H}) = 8.90 + 0.57 \times \mathrm{N2}$ (Pettini & Pagel 2004). However, this calibration remains uncertain, and there are obvious drawbacks to using this index for young galaxies in which AGNs may play a role in defining the emission-line characteristics and in which primary and secondary sources of nitrogen production may lead to mismatches in N/O. For this reason we have chosen to compare populations directly using their N2 measurements [as opposed to (O/H) measured from a range of indicators] to minimize systematic uncertainties arising

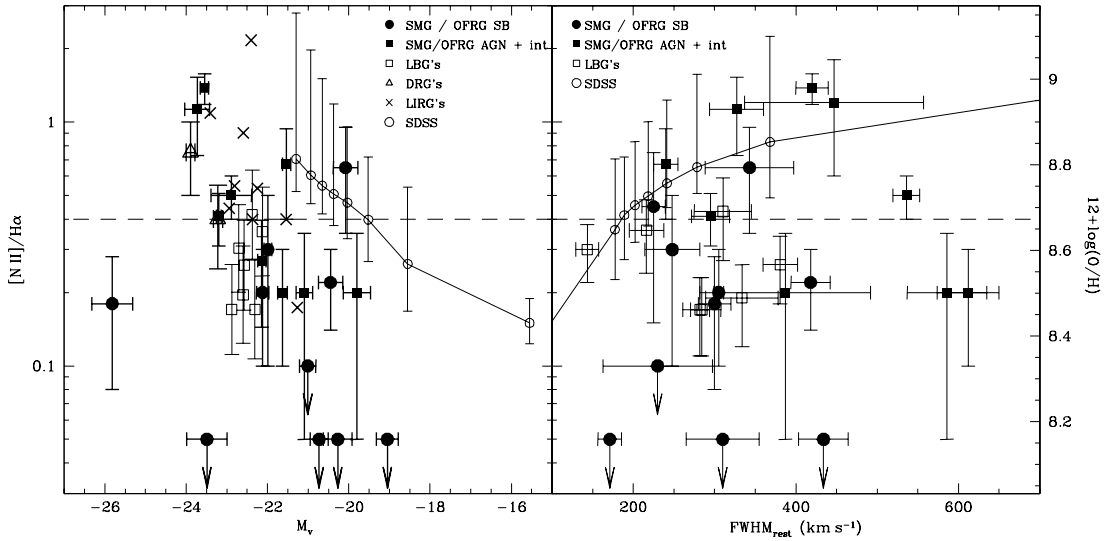

FIG. 9.—*Left*: Metallicity-luminosity relation for SMGs/OFRGs. *Right*: Line width–metallicity relation for the SMGs/OFRGs. The abundance is derived using the N2 index calibration given by Pettini & Pagel (2004). We show two low-redshift samples for comparison, one from the SDSS DR2 (Abazajian et al. 2004) and one for local luminous infrared galaxies (Armus et al. 1989). For a higher redshift comparison sample, we show the metallicities for the $z \sim 2$ UV-selected galaxies from Shapley et al. (2004) and for a near-infrared–selected sample of luminous, $z \sim 2$ galaxies from van Dokkum et al. (2004). The horizontal dashed line represents solar metallicity. The SMGs/OFRGs exhibit a large range in M_V and $\mathrm{FWHM}_{\mathrm{rest}}$, and many have slightly subsolar or solar abundances. Note that these are the observed *V*-band luminosities (uncorrected for reddening; cf. Fig. 7). [*See the electronic edition of the Journal for a color version of this figure.*]

from the calibration from N2 to (O/H). We therefore determine the N2 index for all of the galaxies in our sample and give upper limits where the [N II] emission line is not detected with sufficient significance to measure accurately.

In Figure 9 we show the distribution of M_V versus N2 for SMGs/OFRGs as a proxy for their luminosity-metallicity relation and compare this with similar observations of both local and high-redshift galaxy populations. To calculate the observed rest-frame *V*-band luminosities of the SMGs, we use the photometry from Smail et al. (2004) and fit SEDs based on their observed broadband *IJK* magnitudes, which, at $z \sim 2.4$, corresponds to rest-frame *UBR*, bracketing the *V* band. As Smail et al. (2004) show, the competing effects of dust reddening and fading of the young stellar populations almost cancel each other ($\Delta_{\mathrm{dust}} V \sim 3-4$, $\Delta_{\mathrm{fade}} V \sim 4$ based on fitting the broadband colors of this population). Thus, we expect that the present-day descendants of these galaxies would have absolute luminosities not very dissimilar to those we have estimated (see also Fig. 7). For the comparison samples we convert the rest-frame *B*-band magnitudes for the UV-selected $z \sim 2$ sample from Shapley et al. (2004) using their $(R - K)$ colors to predict the rest-frame *V*-band magnitudes. We also convert the median, 10 and 90 percentile trend lines from a volume-limited ($z < 0.1$) local emission-line galaxy sample from the SDSS DR2 (Abazajian et al. 2004; although we stress that the Sloan aperture only samples the central ~3 kpc of a galaxy at $z = 0.05$ whereas the NIRSPEC slit will sample ~10 kpc at $z = 2.3$). We see at least an order-of-magnitude range in N2 for the SMGs/OFRGs (discounting obvious AGNs), with little correlation between the line index and rest-frame luminosity. The implied median metallicity is slightly below solar and appears to be similar to that inferred for bright, UV-selected galaxies at $z \sim 2$ (Shapley et al. 2004).

To address the competing and uncertain effects of dust reddening and passive fading of the stellar populations on the M_V versus [N II]/Hα plot, we have also constructed an $\mathrm{FWHM}_{\mathrm{H}\alpha}$ versus [N II]/Hα diagram, adopting the $\mathrm{FWHM}_{\mathrm{H}\alpha}$ as a crude proxy for the dynamical mass of the galaxies. As can be seen, the large dynamical masses we inferred for the SMG/OFRG population suggest that their present-day descendants are likely to be luminous and metal-rich (supersolar) systems (as shown by the trends seen in the SDSS data set plotted in Fig. 9). The apparently modest metallicities we measure would then indicate that these systems are seen during an early phase of enrichment, suggesting that they are relatively youthful galaxies and arguing against them undergoing a cycle of repeated short (~10 Myr) bursts of star formation over a relatively extended period (≳1 Gyr; Smail et al. 2003). However, there are other possible explanations for the apparently low metallicities of these galaxies. First, we note that star formation can usually only act to increase a galaxy's metallicity (and therefore N2), and in particular starburst-driven feedback mechanisms are unlikely to preferentially expel large quantities of metals without entraining and expelling associated gas. Only an infall of unenriched material into the galaxy could cause the metallicity and effective heavy-element yield to decrease (e.g., Garrett 2002). Alternatively, if these systems are very young and the halos of the SMGs/OFRGs have yet to coalesce (as suggested by the clear merger/interacting morphologies of many systems), then the metallicities we measure may reflect those of the progenitor components. The similarity of the N2 estimates with those for the UV-selected population at this epoch could then be interpreted as indicating that the SMGs/OFRGs arise from mergers among the UV population. The slightly more evolved descendants of these mergers will be able to retain their enriched gas and so produce a supersolar stellar population. We stress that local calibrations of the N2 index from H II regions can show supersolar metallicities that may not reflect the global abundance in a galaxy. However, since our spectroscopic slit covers most of the area of our galaxies and the measured Hα fluxes suggest substantial star formation, we suggest that the N2 index should provide a fair estimate of the metallicity of the gas in the galaxy as a whole. We caution that the nitrogen abundances that we measure come from primary metal enrichment, whereas the local N/O versus O/H relations suggest that for metal-rich systems the nitrogen

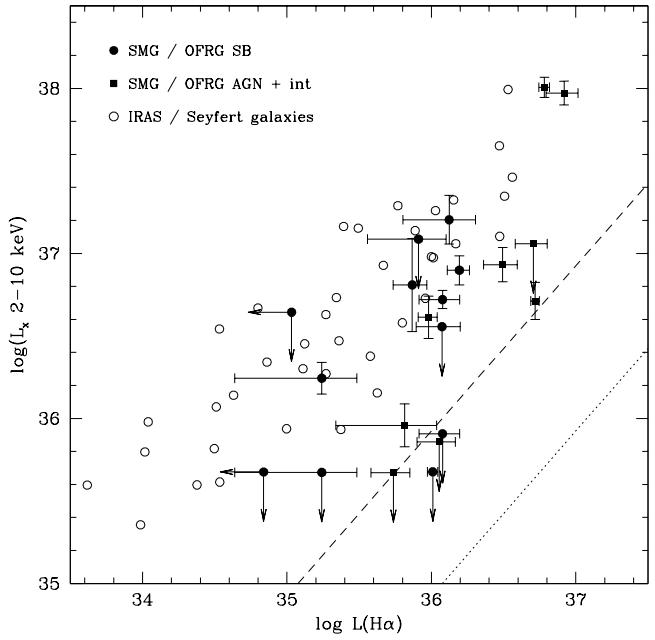

FIG. 10.—Distribution of Hα and X-ray luminosities for the SMGs/OFRGs in our sample as compared to the local *IRAS*-selected Seyfert galaxies from Ward et al. (1988). For the SMG/OFRG sample we plot the total Hα luminosity from both narrow and broad components (if present). We also compare the data to a sample of nearby star-forming galaxies by Ranalli et al. (2003), shown by a dotted line [converting their L(FIR) to L(Hα) assuming that the correlation in § 2 holds], and include the same line but assuming a 10 times suppression of the Hα emission (relative to the far-infrared) as indicated in Fig. 8, shown by a dashed line. The plot shows that some SMGs/OFRGs that are identified as star-forming in the near-infrared (with FWHM $\leq$ 500 km s^{-1} and [N II]/Hα $\lesssim$ 0.7) show 2–10 keV X-ray fluxes consistent with AGN luminosities. It is also interesting to note that some of the SMGs/OFRGs that are spectroscopically classified as AGNs from their near-infrared spectra are not detected in the hard X-ray band. [*See the electronic edition of the Journal for a color version of this figure.*]

is secondary in origin (produced from intermediate-mass stars far removed from the first generation). The evolution of the nitrogen metallicity-luminosity relation might be therefore quite different from that shown for oxygen or other α-elements. We also note that the N2 index is not an ideal metallicity indicator given the presence of an AGN in many of these galaxies, and we look forward to future studies based on [O II], [O III], and Hβ emission lines.

3.7. *X-Ray Comparisons*

Using deep *Chandra* observations of the Hubble Deep Field (HDF), ELAIS N2 field, and SSA13 field (Alexander et al. 2003b; Manners et al. 2003; Mushotzky et al. 2000), it is possible to compare the X-ray and Hα properties of the SMGs/OFRGs that overlap with the *Chandra* coverage. Of the 18 sources that were covered by *Chandra*, 9 were detected in the 2–8 keV hard X-ray band, mostly in the HDF owing to the much deeper X-ray observations available for that field. We convert the observed 2–8 keV flux to a rest-frame 2–10 keV luminosity using $L_X = 4\pi d_L^2 f_X (1+z)^{\Gamma-2}$, which takes into account the *k*-correction (Alexander et al. 2003b), assuming a spectral index $\Gamma = 2$.

In Figure 10 we compare the Hα luminosities from the SMGs/OFRGs to their X-ray luminosities and contrast these with a local sample of *IRAS*-selected Seyfert galaxies analyzed by Ward et al. (1988). We also overlay two lines showing the correlation of $L_{(2-10\,\mathrm{keV})}$ versus L(FIR) from Ranalli et al. (2003). The first line simply converts their L(FIR) to L(Hα) assuming that the relation in § 2 holds, and the second line assumes a further 10 times suppression of the Hα emission (relative to the far-infrared) as indicated by Figure 8.

The distribution of the SMGs/OFRGs in Figure 10 roughly follows that seen for the Ward et al. (1988) sample, *irrespective* of the spectral classification of the SMGs/OFRGs. However, we note that the correlation for local star-forming galaxies from Ranalli et al. (2003), if scaled for the relative underluminosity of Hα in the SMGs/OFRGs, can explain the properties of the least X-ray luminous galaxies; these comprise roughly half of our sample.

The most intriguing galaxies in Figure 10 are those that have high X-ray luminosities ($\log L_X \gtrsim 36.5$) but have rest-frame optical spectral classifications of star formation: the X-ray luminosity in these galaxies probably arises from an AGN that is so highly obscured that either it is hidden in the rest-frame optical spectra (given their modest signal to noise) or we missed the AGN component with our spectroscopic slit in these systems. The presence of a broad-line component in the composite star-forming spectrum in § 3.2 would support the former interpretation.

We also point out that there are six SMGs/OFRGs that are not detected to a flux limit of 1.4×10^{-19} W m^{-2} in the 2 Ms *Chandra* observations of the HDF (two) or 2.2×10^{-18} W m^{-2} in the ELAIS N2 (four) field. While three of these are classified as SBs from their rest-frame optical spectra, three others show some signs of AGNs in the near-infrared spectra (with broad Hα or large [N II]/Hα ratios). The X-ray limits on two of these (SMM J163650.43 and SMM J163706.51) are particularly stringent, yet they show clear AGN signatures in their near-infrared spectra. The detection of broad Hα and lack of X-ray emission are difficult to understand, with these galaxies being almost an order of magnitude fainter in the X-ray wave band than expected from their Hα luminosities. Given the amount of gas available to fuel an AGN in these systems, we conclude that they are likely to be intrinsically low luminosity and probably have low-mass central black holes.

4. CONCLUSIONS

We present the results of near-infrared spectroscopic and narrowband detections or limits on the Hα emission from a sample of 30 ultraluminous, dusty galaxies at $z \sim 1.4-2.7$. The majority of these galaxies come from submillimeter/millimeter surveys, with a small number identified as probable hot, luminous far-infrared sources from their radio emission. We see no difference between the properties of these two samples in any of our diagnostic diagrams, supporting the claimed similarity of the two populations (Chapman et al. 2004b).

We identify the Hα emission in the near-infrared spectra and use the spectra to classify AGNs by flagging galaxies with large [N II]/Hα ratios ($\geq$0.7) and/or large Hα FWHM (>500 km s^{-1}). We find that the ratio of AGN- to star formation–dominated galaxies from the rest-frame optical spectroscopy is roughly 40% : 60%, similar to the proportions estimated from their UV spectra by Chapman et al. (2003a, 2003b, 2004c). By constructing a rest-frame composite spectrum for the entire sample, we find that the average [N II]/Hα ratio is 0.42 $\pm$ 0.05, which suggests that the composite is star formation rather than AGN dominated, although it has an underlying broad-line component. Furthermore, the composite spectra show both Na D absorption and [S II] emission features, although we find no evidence of velocity offsets between these features and the Hα emission. The [S II]/Hα emission ratio in the composite spectrum is 0.10 $\pm$ 0.04, indicating that the spectral properties of our sample are comparable to a LINER or H II region; similar results are found from the spectral classifications of

local ULIRGs (Veilleux & Osterbrock 1987; Veilleux et al. 1995).

We also derive the composite spectrum for those galaxies that, individually, show no signs of an AGN in their near-infrared spectra. This composite has an average [N II]/Hα flux ratio of 0.19 ± 0.05 and $\mathrm{FWHM_{rest}}$ of 400 ± 70 km s^{-1}. However, the most striking result is that the composite spectrum appears to show an underlying broad Hα line with a broad/narrow Hα flux ratio of 0.45 ± 0.20, suggesting that even these galaxies may host a low-luminosity AGN that is undetectable in our modest signal-to-noise ratio spectroscopy.

In seven of the systems with spectroscopic observations we find velocity structure in the Hα emission line. By comparison with high-resolution broadband imaging, we identify these galaxies as multicomponent (probably interacting) systems with typical velocity offsets between components of 100–600 km s^{-1}. This is not surprising since locally many far-infrared luminous galaxies appear to be disturbed/interacting systems. Assuming that these are merging systems with random orientations of their orbits on the sky, we estimate a typical mass of $(1.5 \pm 0.9) \times 10^{11}\ M_{\odot}$. We obtain a similar estimate from the Hα line widths of the whole sample. These estimates are comparable to the dynamical mass estimates from CO observations of a subset of these systems.

In all of the galaxies, we have attempted to deconvolve any broad component to the Hα line (which comes from an accretion disk around a central supermassive black hole) from the narrow-line Hα flux (which comes from the star-forming regions). Using the narrow-line Hα flux, we compare the SFRs of the SMGs/OFRGs as compared to the SFR derived from the far-infrared emission. The SFR(Hα) versus SFR(FIR) correlation shows a large scatter, with the SFR(Hα) typically a factor of 10 less than what we would expect from their far-infrared luminosities. Most of this scatter, however, can be explained by the reddening in these systems (estimated from their broadband photometry in Smail et al. 2004). The suppression of the Hα flux is therefore attributed to both heavily obscured galaxies and a diverse range of morphologies. The average SFR derived from Hα for the SMGs/OFRGs in our sample is $94 \pm 20\ M_{\odot}$ yr^{-1} (uncorrected for extinction). Since the continuum extinction correction at 6563 Å is $\sim$2.5 mag, the total inferred SFR of these galaxies is expected to be $\sim$1000 $M_{\odot}$ yr^{-1}, comparable to that seen in the far-infrared. We also compare the SFR properties for our high-redshift sample to local very luminous/ultraluminous galaxy samples and find that the scatter within our high-redshift SMGs/OFRGs and the distribution of equivalent widths are comparable to those of local ultraluminous/very luminous galaxy samples. This suggests a similar range of obscured/unobscured activity in the distant population to that seen locally, although with a higher proportion of the star formation completely obscured from view.

Using the N2 index, we have investigated the chemical abundances of these galaxies and find that the N2 indices for the SMGs/OFRGs suggest that they have slightly subsolar metallicities, similar to recent results from UV-selected galaxies at these early epochs (Shapley et al. 2004). However, we note that the N2 indicator may not be a reliable metallicity indicator for this population, especially in the presence of an AGN. We find that the SMGs/OFRGs in our sample display a large range in [N II]/Hα versus M_V or $\mathrm{FWHM_{rest}}$ (which we use as a proxy for their dynamical masses).

For the galaxies that are in the HDF, ELAIS N2 field, and SSA13 field we use their X-ray properties in order to further classify the galaxies. The SMGs/OFRGs classified as AGNs on the basis of their near-infrared spectra broadly follow the correlation seen between X-ray and Hα luminosities for local Seyfert 2 galaxies (Ward et al. 1988). We find that a subset of galaxies that are spectroscopically classified as star-forming in the near-infrared have high X-ray luminosities, suggesting that they host highly obscured AGNs. Likewise, a small number of near-infrared spectroscopically classified AGNs are undetected in deep *Chandra* observations. We conclude that these galaxies are likely to be intrinsically low luminosity and probably have low-mass central black holes.

With observations of the Hα emission from these SMGs/OFRGs at $z \sim 2$ we can at last start to directly compare these galaxies to similarly distant UV-selected systems. We find that, as expected, the SFR(Hα) for our sample is nearly an order of magnitude higher than that found in $z \sim 2$ UV-selected galaxies by Erb et al. (2003) [who find an average SFR(Hα) of $21 \pm 3\ M_{\odot}$ yr^{-1}, even after their sample is corrected for extinction]. Similarly, the line widths and dynamical information suggest that the halos of a typical SMG/OFRG may be up to 5 times more massive than the UV-selected population. We also find a higher rate of AGN activity in the SMGs/OFRGs, suggesting the presence of actively fueled and growing supermassive black holes in these galaxies. However, somewhat surprisingly, we find similar metallicities for the UV-selected and more massive far-infrared luminous populations. We suggest that this may be explained if the SMGs/OFRGs are relatively youthful, with their deepening potential wells not yet sufficiently organized to retain a larger fraction of the enriched material from their star formation activity.

Overall our observations suggest that the high-redshift SMG/OFRG population shares many of the characteristics of similar (but somewhat less luminous) far-infrared galaxies identified in the local universe. This includes the Hα equivalent widths, the proportion of obvious AGNs, and the typical optical spectral classification. Previous work has demonstrated the preponderance of merger-like morphologies in the two populations and the similarity of their rest-frame optical luminosities. However, there remain differences, with proportionally more highly obscured activity in the high-redshift population, apparently larger dynamical mass, lower metallicities, and higher gas fractions on 10 kpc scales.

We conclude that the SMGs/OFRGs in our sample represent a population of young, massive merging/interacting systems, the results of which cause high instantaneous bursts of (highly obscured) star formation and actively fueled AGN activity. Although these bursts are brief, they can form all of the stars in an L^* galaxy and in doing so will raise the metallicity of these systems closer to that required by observations of their likely present-day descendants: luminous elliptical galaxies.

We thank the referee for his constructive comments and suggestions that significantly improved the content of this paper. We would like to thank David Gilbank for adapting I-PIPE and extensive help reducing the IRTF narrowband imaging and Mike Balogh, Chris Miller, and Bob Nichol for providing the SDSS catalogs in a usable format. We acknowledge useful conversations or help from Dave Alexander, Carlton Baugh, Richard Bower, Chris Done, Dave Gilbank, Cedric Lacey, Max Pettini, Alice Shapley, Chris Simpson, Kaz Sekiguchi, and Tadafumi Takata. A. M. S. acknowledges support from PPARC, I. R. S. acknowledges support from the Royal Society, and A. W. B. acknowledges support from NSF AST 02-05937 and the Alfred Sloan Foundation.

REFERENCES

Abazajian, K., et al. 2004, AJ, 128, 502 (SDSS Collaboration)
Adelberger, K. L., Steidel, C. C., Shapley, A. E., & Pettini, M. 2003, ApJ, 584, 45
Alexander, D. M., et al. 2003a, AJ, 125, 383
———. 2003b, AJ, 126, 539
Armus, L., Heckman, T. M., & Miley, G. K. 1989, ApJ, 347, 727
Barger, A. J., Cowie, L. L., Smail, I., Ivison, R. J., Blain, A. W., & Kneib, J.-P. 1999, AJ, 117, 2656
Baugh, C. M., Lacey, C. G., Frenk, C. S., Granato, G. L., Silva, L., Bressan, A., Benson, A. J., & Cole, S. 2004, MNRAS, submitted
Blain, A. W., Chapman, S. C., Smail, I., & Ivison, R. J. 2004, ApJ, in press
Blain, A. W., Smail, I., Ivison, R. J., & Kneib, J.-P. 1999, MNRAS, 302, 632
Bolzonella, M., Miralles, J.-M., & Pelló, R. 2000, A&A, 363, 476
Calzetti, D., Kinney, A. L., & Storchi-Bergmann, T. 1994, ApJ, 429, 582
Chapman, S. C., Blain, A. W., Ivison, R. J., & Smail, I. 2003a, Nature, 422, 695
Chapman, S. C., Blain, A. W., Smail, I., & Ivison, R. J. 2004a, ApJ, in press
Chapman, S. C., Richards, E. A., Lewis, G. F., Wilson, G., & Barger, A. J. 2001, ApJ, 548, L147
Chapman, S. C., Smail, I., Blain, A. W., & Ivison, R. J. 2004b, ApJ, in press
———. 2004c, ApJ, in press
Chapman, S. C., Windhorst, R., Odewahn, S., Yan, H., & Conselice, C. 2003b, ApJ, 599, 92
Condon, J. J., Anderson, M. L., & Helou, G. 1991, ApJ, 376, 95
Cowie, L. L., Barger, A. J., & Kneib, J. P. 2002, AJ, 123, 2197
Dawson, S., McCrady, N., Stern, D., Eckart, M. E., Spinrad, H., Liu, M. C., & Graham, J. R. 2003, AJ, 125, 1236
Denicolo, G., Terlevich, R., & Terlevich, E. 2002, MNRAS, 330, 69
Dey, A., Graham, J. R., Ivison, R. J., Smail, I., Wright, G. S., & Liu, M. C. 1999, ApJ, 519, 610
Dopita, M. A., Pereira, M., Kewley, L. J., & Capaccioli, M. 2002, ApJS, 143, 47
Downes, D., & Solomon, P. M. 2003, ApJ, 582, 37
Erb, D. K., Shapley, A. E., Steidel, C. C., Pettini, M., Adelberger, K. L., Hunt, M. P., Moorwood, A. F. M., & Cuby, J. 2003, ApJ, 591, 101
Faber, S. M., & Jackson, R. E. 1976, ApJ, 204, 668
Ferland, G. J., & Osterbrock, D. E. 1986, ApJ, 300, 658
Flores, H., Hammer, F., Elbaz, D., Cesarsky, C. J., Liang, Y. C., Fadda, D., & Gruel, N. 2004, A&A, 415, 885
Franceschini, A., et al. 2003, A&A, 403, 501
Frayer, D. T., Armus, L., Scoville, N. Z., Blain, A. W., Reddy, N. A., Ivison, R. J., & Smail, I. 2003, AJ, 126, 73
Frayer, D. T., et al. 1999, ApJ, 514, L13
Garnett, D. R., Shields, G. A., Skillman, E. D., Sagan, S. P., & Dufour, R. J. 1997, ApJ, 489, 63
Garrett, M. A. 2002, A&A, 384, L19
Genzel, R., Baker, A. J., Tacconi, L. J., Lutz, D., Cox, P., Guilloteau, S., & Omont, A. 2003, ApJ, 584, 633
Giavalisco, M., et al. 2004, ApJ, 600, L93
Hawarden, T. G., Leggett, S. K., Letawsky, M. B., Ballantyne, D. R., & Casali, M. M. 2001, MNRAS, 325, 563
Heckman, T. M., Lehnert, M. D., Strickland, D. K., & Armus, L. 2000, ApJS, 129, 493
Ivison, R. J., Smail, I., Barger, A. J., Kneib, J.-P., Blain, A. W., Owen, F. N., Kerr, T. H., & Cowie, L. L. 2000, MNRAS, 315, 209
Ivison, R. J., Smail, I., Frayer, D. T., Kneib, J.-P., & Blain, A. W. 2001, ApJ, 561, L45
Ivison, R. J., Smail, I., Le Borgne, J.-F., Blain, A. W., Kneib, J.-P., Bezecourt, J., Kerr, T. H., & Davies, J. K. 1998, MNRAS, 298, 583
Ivison, R. J., et al. 2002, MNRAS, 337, 1
Jørgensen, I., Franx, M., Hjorth, J., & van Dokkum, P. G. 1999, MNRAS, 308, 833
Jørgensen, I., Franx, M., & Kjærgaard, P. 1995a, MNRAS, 273, 1097
———. 1995b, MNRAS, 276, 1341
Kennicutt, R. C., Jr. 1998, ARA&A, 36, 189
Kneib, J., van der Werf, P. P., Kraiberg Knudsen, K., Smail, I., Blain, A., Frayer, D., Barnard, V., & Ivison, R. 2004, MNRAS, 349, 1211
Lamareille, F., Mouhcine, M., Contini, T., Lewis, I., & Maddox, S. 2004, MNRAS, 350, 396
Leitherer, C., & Heckman, T. M. 1995, ApJS, 96, 9
Lilly, S. J., Carollo, C. M., & Stockton, A. N. 2003, ApJ, 597, 730
Lilly, S. J., Eales, S. A., Gear, W. K. P., Hammer, F., Le Fevre, O., Crampton, D., Bond, J. R., & Dunne, L. 1999, ApJ, 518, 641
Lutz, D., Veilleux, S., & Genzel, R. 1999, ApJ, 517, L13
Manners, J. C., et al. 2003, MNRAS, 343, 293
McLean, I. S., et al. 1998, Proc. SPIE, 3354, 566
Moorwood, A. F. 1997, Proc. SPIE, 2871, 1146
Mushotzky, R. F., Cowie, L. L., Barger, A. J., & Arnaud, K. A. 2000, Nature, 404, 459
Neri, R., et al. 2003, ApJ, 597, L113
Pettini, M., & Pagel, B. E. J. 2004, MNRAS, 348, L59
Pettini, M., Shapley, A. E., Steidel, C. C., Cuby, J., Dickinson, M., Moorwood, A. F. M., Adelberger, K. L., & Giavalisco, M. 2001, ApJ, 554, 981
Phillips, A. C. 1993, AJ, 105, 486
Poggianti, B. M., & Wu, H. 2000, ApJ, 529, 157
Ranalli, P., Comastri, A., & Setti, G. 2003, A&A, 399, 39
Roche, P. F., et al. 2003, Proc. SPIE, 4841, 901
Rupke, D. S., Veilleux, S., & Sanders, D. B. 2002, ApJ, 570, 588
Shapley, A. E., Erb, D. K., Pettini, M., Steidel, C. C., & Adelberger, K. L. 2004, ApJ, 612, 108
Shapley, A. E., Steidel, C. C., Pettini, M., & Adelberger, K. L. 2003, ApJ, 588, 65
Shure, M., et al. 1993, BAAS, 25, 1468
Simpson, C., Dunlop, J. S., Eales, S. A., Ivison, R. J., Scott, S. E., Lilly, S. J., & Webb, T. M. A. 2004, MNRAS, 353, 179
Smail, I., Chapman, S. C., Blain, A. W. & Ivison, R. J., 2004, ApJ, 616, 71
Smail, I., Ivison, R. J., Blain, A. W., & Kneib, J. P. 2002, MNRAS, 331, 495
Smail, I., Ivison, R. J., Gilbank, D. G., Dunlop, J. S., Keel, W. C., Motohara, K., & Stevens, J. A. 2003, ApJ, 583, 551
Storchi-Bergmann, T., Calzetti, D., & Kinney, A. L. 1994, ApJ, 429, 572
Tecza, M., et al. 2004, ApJ, 605, L109
Tully, R. B., & Fisher, J. R. 1977, A&A, 54, 661
van Dokkum, P., et al. 2004, ApJ, 611, 703
Veilleux, S., Kim, D.-C., & Sanders, D. B. 1999, ApJ, 522, 113
Veilleux, S., Kim, D.-C., Sanders, D. B., Mazzarella, J. M., & Soifer, B. T. 1995, ApJS, 98, 171
Veilleux, S., & Osterbrock, D. E. 1987, ApJS, 63, 295
Wang, W. H., Cowie, L. L., & Barger, A. J. 2004, ApJ, 613, 655
Ward, M. J., Done, C., Fabian, A. C., Tennant, A. F., & Shafer, R. A. 1988, ApJ, 324, 767
Yan, L., McCarthy, P. J., Freudling, W., Teplitz, H. I., Malumuth, E. M., Weymann, R. J., & Malkan, M. A. 1999, ApJ, 519, L47
Zaritsky, D., Kennicutt, R. C., Jr., & Huchra, J. P. 1994, ApJ, 420, 87